# Modeling rainfall-induced landslide using the concept of local factor of safety: Uncertainty propagation and sensitivity analysis

Rashad Abbasov, Marwan Fahs, Anis Younes, Hossein Nowamooz, Knut Jørgen Måløy, Renaud Toussaint

Computers and Geotechnics 167 (2024) 106102

Contents lists available at ScienceDirect

Computers and Geotechnics

journal homepage: www.elsevier.com/locate/compgeo

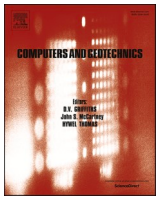

Research Paper

# Modeling rainfall-induced landslide using the concept of local factor of safety: Uncertainty propagation and sensitivity analysis

Rashad Abbasov [a], Marwan Fahs [a,*], Anis Younes [a], Hossein Nowamooz [b], Knut Jørgen Måløy [c], Renaud Toussaint [a,c]

[a] Université de Strasbourg, CNRS, ENGEES, Institut Terre et Environnement de Strasbourg, UMR 7063, F-67000 Strasbourg, France
[b] ICUBE, UMR 7357, CNRS, INSA de Strasbourg, 24 boulevard de la Victoire, 67084 Strasbourg, France
[c] PoreLab, The Njord Centre, Department of Physics, University of Oslo, Oslo, Norway

ARTICLE INFO

*Keywords:*
Rainfall-induced landslides
Slope stability
Hydro-mechanical modeling
Local factor of safety
Uncertainty analysis

ABSTRACT

Rainfall-induced landslides (RILS) are commonly investigated using hydro-mechanical models with the concept of local factor of safety. The inputs of these models are usually prone to uncertainties. An uncertainty analysis is required to investigate how uncertainties propagate through the model and impact the predictions. An appropriate strategy for uncertainty propagation analysis is suggested in this work to deal with nonlinearity and high dimensionality of RILS problems. It proceeds by performing a sensitivity analysis in two steps. A screening technique is first applied to eliminate insignificant parameters. Then, a global sensitivity analysis is performed to rank the parameters by order of importance. The Sobol indices are used as sensitivity metrics. The polynomial chaos expansion is used to compute the Sobol indices. The proposed strategy is first applied to a hypothetical benchmark and then to a more realistic configuration where prior knowledge of parameters and type of soil are considered. The results show that, when prior knowledge of soil is available, the most important parameters are the coefficient of cohesion, friction angle and air entry pressure head, respectively. The results also show that 10% uncertainty on these parameters leads to about 20% uncertainty on the prediction of slope stability.

## 1. Introduction

Landslides are geological processes that correspond to the movement of soil and rocks down a slope (Highland & Bobrowsky, 2008). Such erosional process occurs due to human activity (irrigation, artificial vibration, deforestation, mining &, etc.) and natural phenomena (volcanic activity, earthquakes, heavy rainfalls, and others). All these activities trigger the failure of mechanical balance as shear stress overcomes shear strength. Landslides have a wide variety of movements, for instance, falls, topples, slides (rotational, translational), lateral spreads, flows, and complex (combines two or more types) (Hungr et al., 2014). Due to climate change, intensive rainfall events have become more frequent, and the occurrence of rainfall-induced landslides (RILS) is becoming frequent (Haque et al., 2016). During intensive rainfall events, the increase of water saturation in soil negatively affects slope stability (Travelletti et al., 2011, 2012). Infiltration of water increases the body load, and pore water pressure oppositely decreases suction stress, effective stress, and affects the shear strength, with an increase followed by a decrease of cohesion with saturation (Jouniaux et al., 2020; Mitarai & Nori, 2006). The reduced soil strength is a potential risk for slope failure (Moradi et al., 2018). Landslides are serious geologic hazards that can cause widespread damages, for example, property losses, infrastructure destruction, injury, and death. Landslides can be a crucial factor in degassing of volcanic mountains, lake bottoms, or marine sediments that can affect the environment on a bigger scale. As a prime example, the emission of large volumes of greenhouse gases led to mass extinction during the Permian period (Wirth et al., 2013).

The main interest of this work is RILS (Shao et al., 2015). It is impossible to prevent such a naturally occurring hazard, but it is possible to mitigate potential risks through modeling. Multi-physics modeling is an effective tool that can help in predicting the risk of landslides. This requires coupling hydro-mechanical processes (Chiu et al., 2019). As soil is usually unsaturated or partially saturated, the flow processes can be modeled with Richard's equation, combining Darcy's law, mass conservation, and constitutive relations expressing permeability and pressure head as functions of saturation (Toussaint

* Corresponding author.
*E-mail address:* fahs@unistra.fr (M. Fahs).

https://doi.org/10.1016/j.compgeo.2024.106102
Received 19 July 2023; Received in revised form 12 January 2024; Accepted 13 January 2024
Available online 24 January 2024

et al., 2012; Ayaz et al., 2020; Moura et al., 2015). Mechanical processes are simulated with the equation of local equilibrium coupled to the linear elasticity model. The flow and mechanical equations are coupled because the increase of water content, due to infiltration, leads to an extra load on the soil. The gravity term in the local equilibrium equation depends on the water content, which is one of the primary unknowns of Richard's equation. Effective stress is also a function of water pressure (Ben Zeev et al. 2020, 2017,; Clément et al., 2018; Goren et al., 2013).

Landslide susceptibility can be investigated using an indicator that measures slope stability. Though several approaches have been made to assess slope stability, this study will focus on the Local Factor of Safety (LFS) method (Tsai, 2008). The LFS concept is the Coulomb stress-field-based method. It is defined as the ratio of resisting shear strength ($\tau^*$) to gravitationally driven shear stress ($\tau$) in the direction of failure (Moradi et al., 2018; Lu et al., 2012; Tsai & Wang, 2011). The global factor of safety has been widely used in the literature (Baum et al., 2010; Chiu et al., 2019). It is based on assigning a global metric to analyze the slope instability by assuming an infinite slope, which is based on the idea that the failure occurs along a plane parallel to the slope surface. The global factor of safety is expressed as a function of the slope angle, effective cohesion coefficient, friction angle, and water pressure. It can be easily calculated, but its reliability is questionable when the infinite slope assumption is invalid. It does not allow for identifying the location of the rupture surface and the area where the failure initiates (Lu et al., 2012). The LFS is evaluated at each point of the domain (Lu et al., 2012). It can be expressed in terms of the eigenvalues of the effective stress tensor and some soil properties (i.e. effective cohesion coefficient and friction angle). The LFS concept is coherent with the global factor of safety but provides more details about instability initiation and the location and geometry of the potential failure surface (Lu et al., 2012). LFS does not require initial thoughts about the failure plane's location and shape and can be applied to unstructured meshes. These features bring an advantage to LFS over other slope stability assessment methods (Moradi et al., 2018).

Hydro-mechanical models and the LFS concept are widely used for understanding the processes of RILS and in developing early warning systems (Menon & Kolathayar, 2022; Mandal & Sarkar, 2021; Greco & Pagano, 2017). The approach based on LFS has some drawbacks. Its application is limited to elastic materials and local point-by-point analysis. Despite these simplifications, LFS provides a more precise criterion for investigating coupled hydro-mechanical processes than other approaches. Furthermore, LFS can be calculated automatically in the model. This renders it interesting for uncertainty analysis, which is the main goal of this work, as it will be explained later. Moreover, Lu et al., (2012) discussed the validity of the LFS concept and showed that its results for stability analysis are in good agreement with other conventional concepts.

In real applications, the input parameters are often prone to uncertainties that could be related to measurements, fitting procedure, or imperfect knowledge of system conditions (Yang et al., 2022; Rajabi et al., 2020; Yang et al., 2018). In particular, the properties of soils are subject to uncertainty because they are identified by calibrating the model against observations with insufficient data that could suffer from noises (Koohbor et al., 2019). These uncertainties in input parameters propagate through the model, affect the model outputs, and negatively impact the reliability of the model predictions. When the models are used for developing warning systems, the uncertain model's predictions can lead to unreliable warning information. Therefore, in modeling-based studies of landslide susceptibility, there is a vital importance in performing an uncertainty analysis (UA) to understand how uncertainties in the inputs propagate through the model and reach the outputs.

Despite its vitality, studies on UA for landslide models are scarce. Ji et al. (2021), Pan et al. (2021), Kasama et al. (2021), and Khalaj et al. (2020) used a stochastic approach to perform an UA of seismically induced slope displacements by considering uncertain seismic ground motions. In the case of RILS, Cai et al. (2017), Johari and Talebi (2019) and Yang et al. (2022) performed an UA by considering uncertain soil hydraulic properties. Almeida et al. (2017) performed an UA by assuming the slope angle and rainfall rate as uncertain inputs. Liao and Ji (2021) presented a time dependent reliability analysis by assuming uncertain hydraulic conductivity and soil shear strength. To the best of our knowledge, there is no detailed study on UA for RILS, integrating all hydraulic and mechanical parameters of soils. Indeed, as the number of parameters is relatively high and the forward hydro-mechanical model is nonlinear and highly consuming in CPU time, and because UA requires hundreds of runs, performing a full UA for RILS is a challenging task. It requires a fast-forward model and a robust and efficient algorithm for uncertainty analysis.

This work aims at suggesting an appropriate and efficient strategy for performing UA for RILS. The newly suggested strategy consists in combining an uncertainty propagation analysis that allows for ranking the parameters by order of importance, followed by an uncertainty quantification analysis that allows for evaluating uncertainties on model outputs. Specific techniques are implemented to deal with the complexities related to the computational costs, knowing the nonlinearity and high dimensionality of the problem of RILS. The new strategy consists of *i)* reducing the dimensionality of the problem by performing a preliminary screening analysis, *ii)* using a surrogate model to replace the highly consuming hydro-mechanical model, *iii)* using an efficient forward model, *iv)* selecting an appropriate quantities of interest and relevant sensitivity metrics and *v)* performing the uncertainty quantification analysis using the surrogate model. Thus, to reduce the number of runs of the forward model, the new strategy consists in coupling a screening technique with the global sensitivity analysis (GSA) (Sahu et al., 2023). A preliminary sensitivity analysis, developed with the screening technique, allows for reducing the model's dimensionality by identifying the most significant parameters from a well-designed design of experiments and by neglecting interaction between parameters. These parameters are then ranked according to their significance based on a GSA (Sudret, 2008; Fajraoui et al., 2017; Fang and Su, 2020; Guo et al., 2021). GSA is used to determine the key input parameters responsible for output variability. We used a variance-based technique for the GSA with the Sobol indices as sensitivity indicators (Sobol', 1993; Glen et al. 2012). Sobol indices are variance-based metrics of sensitivity (Sobol', 1993). GSA with variance-based techniques and Sobol indices have gained increasing interest in applications related to coupled processes in soils (Fajraoui et al., 2017; Rajabi et al., 2020; Sandoval et al., 2022). It allows for evaluating the interaction between parameters. GSA with a variance-based technique has never been applied to RILS. One of the objectives of this work is to evaluate the performance of this technique in such a case. The evaluation of the Sobol indices requires many runs of the forward model that could render the GSA impractical. To avoid this issue and optimize the computational costs of the GSA, we use a surrogate model that can replace the original hydro-mechanical forward model in the evaluation of the Sobol indices. Among different surrogate approaches, we use the polynomial chaos expansions (PCEs) because they allow for a forward evaluation of the Sobol indices from the polynomial coefficients. PCEs can be accurately used for uncertainty quantification. An efficient forward model is used to generate samples required for building the PCEs. The model is developed using the COMSOL® finite element package with an adaptive time-stepping technique that significantly reduces CPU time. One of the challenges of an UA is the selection of the quantities of interest. We tested different outputs in order to provide relevant quantities of interest that could reflect the physical processes. Once the most significant parameters are identified, the PCE surrogate model is used for uncertainty quantification via a stochastic approach. The performance of the proposed UA strategy is investigated by applying it to a benchmark of RILS, commonly used in the literature (Shao et al., 2015; Moradi et al., 2018). It deals with a hypothetical case at a 100 m scale and with heterogeneous soil. Hydrodynamic and mechanical properties of soil are assumed

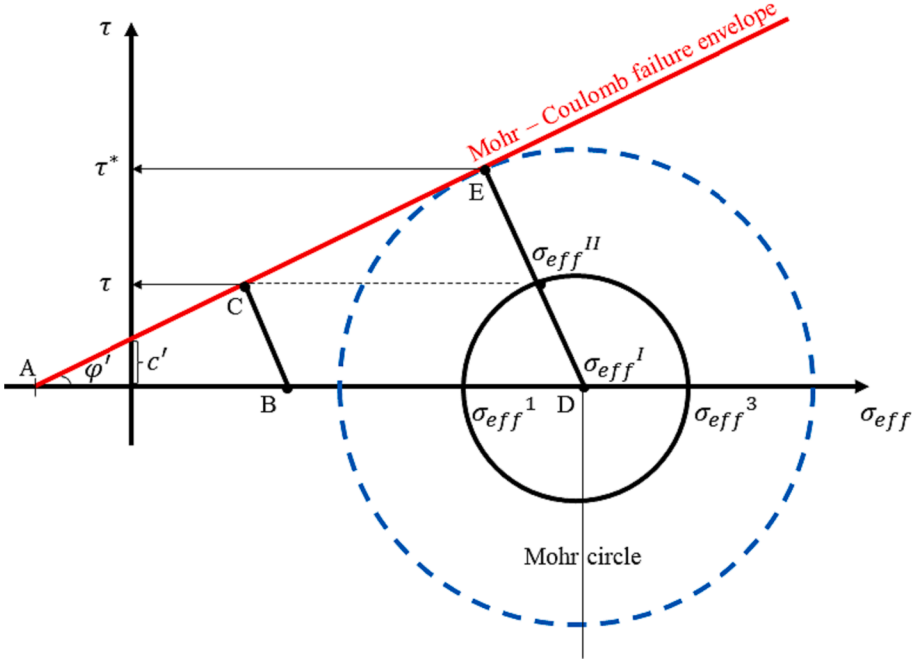


**Fig. 1.** The Mohr circle and Mohr-Coulomb failure envelope used for the evaluation of the LFS. $\sigma_{eff}$ and $\tau$ represent the absolute value of the normal and shear stresses.

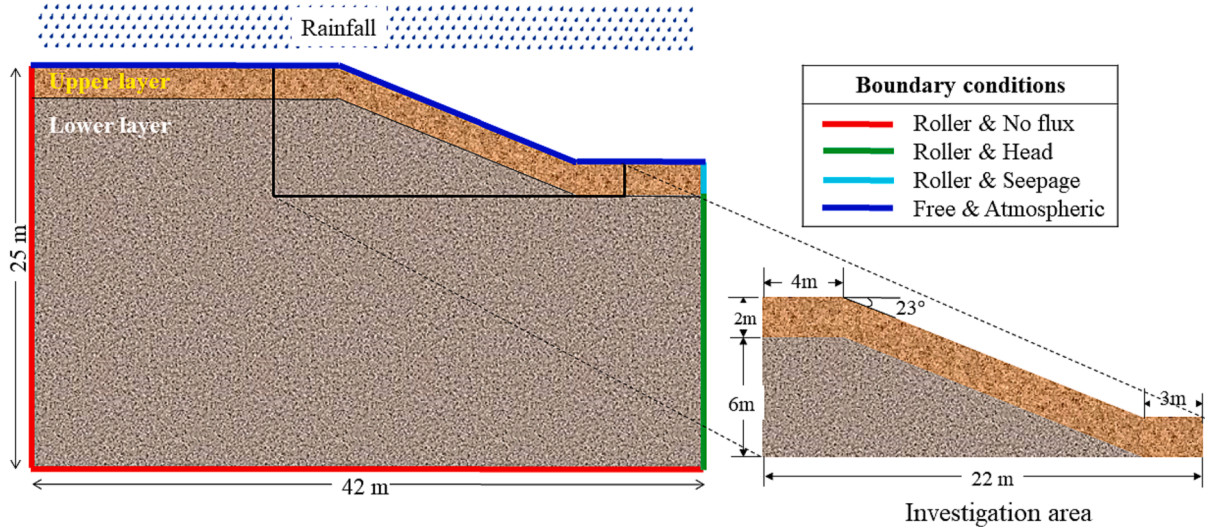


**Fig. 2.** The geometry of the domain and the investigation area as well as the corresponding boundary conditions.

to be uncertain and the impact of this uncertainty on the LFS is evaluated. We also apply the proposed UA strategy to a more realistic configuration where the wetting branch of the retention curves is taken into account an prior knowledge about some parameters and type of soil are considered.

## 2. Mathematical and numerical models

### 2.1. Governing equations: Hydro-mechanical model

The motion of fluids in unsaturated porous media is described by the Richards equation which combines the continuity equation and Darcy's law.

$$\frac{\partial\theta}{\partial t}+\nabla.\boldsymbol{q}=0 \tag{1}$$

$$\boldsymbol{q}=-K(h)\nabla H \tag{2}$$

where $\theta[-]$ is the volumetric water content, $q[m.s^{-1}]$ is Darcy's velocity, $h[m]$ is the pressure head, $H[m]$ is the total hydraulic head ($H=h+z$), $z[m]$ is the depth taken positive upward, and $K[m.s^{-1}]$ is the hydraulic conductivity of the unsaturated soil.

The Brooks and Corey model is used as constitutive relations between the hydraulic head, effective saturation, volumetric water content, and hydraulic conductivity (Shao et al., 2015; Lu *et al.*, 2012). This model is given by:

$$S_e=\frac{\theta(h)-\theta_r}{\theta_s-\theta_r}=\begin{cases}|\alpha_{BC}\cdot h|^{-n_{BC}} if \alpha_{BC}\cdot h<-1\\ 1 if \alpha_{BC}\cdot h\geq -1\end{cases} \tag{3}$$

$$K(h)=K_s\cdot(S_e)^{\swarrow_{BC}+2+\frac{2}{n_{BC}}} \tag{4}$$

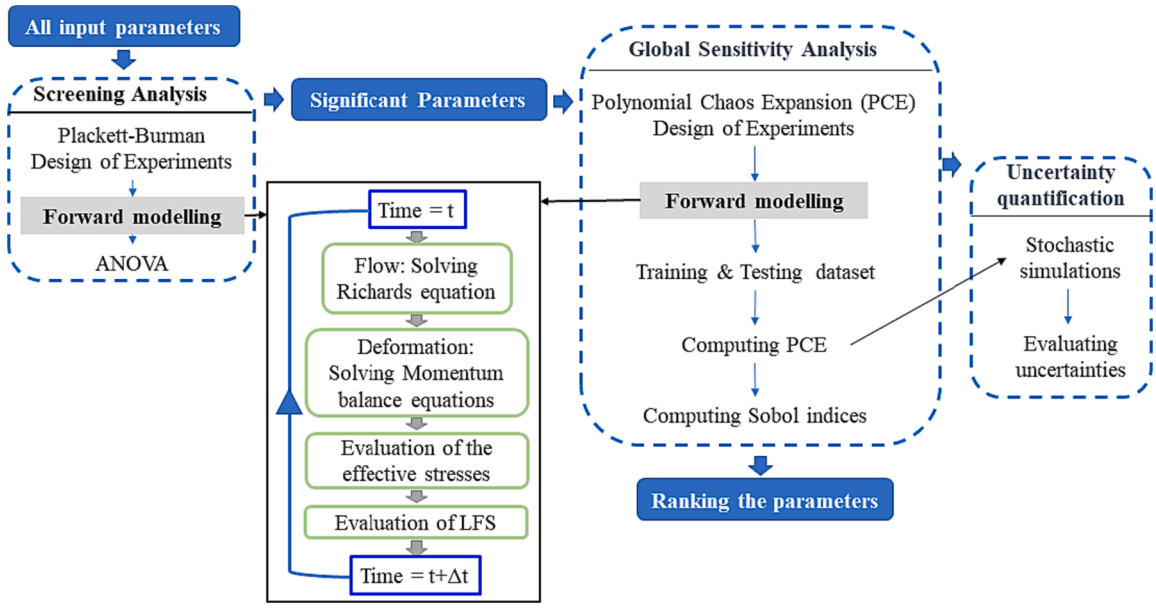


**Fig. 3.** Representation of workflow of the uncertainty analysis (ANOVA is Analysis of Variance).

**Table 1**
Hydrodynamic and mechanical parameters for the soil layers.

| Symbol | Parameter | Units | Upper layer | Lower layer |
|---|---|---|---|---|
| $\theta_s$ | Saturated water content | – | 0.412 | 0.385 |
| $\theta_r$ | Residual water content | – | 0.041 | 0.09 |
| $K_S$ | Saturated hydraulic conductivity | cm/h | 2.59 | 0.06 |
| $\rho_w$ | Density of water | kg/m$^3$ | 1000 | |
| $\alpha_{BC}$ | Brooks-Corey fitting parameters | 1/cm | 0.068 | 0.027 |
| $n_{BC}$ | | – | 0.322 | 0.131 |
| $l_{BC}$ | | – | 1 | |
| $\rho_s$ | Density of solid grains | kg/m$^3$ | 2636 | |
| $E$ | Young's modulus | MPa | 10 | |
| $N$ | Poisson's ratio | – | 0.35 | |
| $\varphi'$ | Friction angle | ○ | 35 | |
| $c'$ | Effective cohesion | kPa | 3 | 6 |

Where $S_e[-]$ is the effective saturation, $\theta_s[-]$ is the water content at saturation which is equal to porosity, $\theta_r[-]$ is the residual water content, $\alpha_{BC}[m^{-1}]$ represents the air entry pressure head, $n_{BC}[-]$ and $\ell_{BC}[-]$ characterize pore size distribution in soil and tortuosity, respectively, and $K_s[m.s^{-1}]$ is the hydraulic conductivity of soil at saturation.

The deformation processes are described with linear momentum equilibrium with a gravity term depending on the water content. (Been Zeev et al., 2020; Goren et al., 2013; Niebling et al., 2010,2012). In this work, we adopt the approach implemented in the hillslope cube module, widely used in the literature (Yang et al. 2022). The approach is based on the evaluation of a linear elastic stress tensor to evaluate stress changes related to the change of soil weight, and then applies the pore water pressure to evaluate an effective stress required for soil stability (Moradi et al., 2018; Shao et al., 2015; Yang et al. 2022). This assumption is necessary for the development of the model with COMSOL® and it allows for reducing the computational cost of the simulations. The linear momentum equilibrium equation is expressed as follows:

$$\nabla.(\boldsymbol{\sigma}) + ((\rho_s(1-\theta_s) + \rho_w\theta)\boldsymbol{g} = 0 \tag{5}$$

where $\boldsymbol{\sigma}[kg.m^{-1}.s^{-2}]$ is the stress tensor, $\rho_s[kg.m^{-3}]$ is the density of the solid grains of soil, $\rho_w[kg.m^{-3}]$ is the density of water and $\boldsymbol{g}[m.s^{-2}]$ is the gravity.

Under the assumption of linear-elastic material, the stress tensor can be expressed as a function of strain tensor using Hooke's law.

### 2.2. the local factor of safety

$LFS[-]$ is defined as the ratio of resisting shear strength ($\tau^*[kg.m^{-1}.s^{-2}]$) to gravitationally driven shear stress ($\tau[kg.m^{-1}.s^{-2}]$) in the failure direction, according to the Mohr-Coulomb criterion (Lu *et al.*, 2012, Iverson & Reid, 1992).

$$LFS = \frac{\tau^*}{\tau} \tag{6}$$

Calculation of LFS is based on the effective stress tensor. In this work, we use the unified effective stress suggested and validated by Lu and Likos (2006) and Lu et al. (2010). The unified effective stress field is given as the difference between the stress tensor ($\sigma$) and the suction stress:

$$\boldsymbol{\sigma}_{eff} = \boldsymbol{\sigma} - \chi\rho_w g h.\boldsymbol{I} \tag{7}$$

Where $\boldsymbol{\sigma}_{eff}[kg.m^{-1}.s^{-2}]$ is the unified effective stress tensor, $\boldsymbol{I}[-]$ is the identity tensor, $\chi[-]$ is Bishop parameter. The general relation between effective and total stresses was given by Bishop (1959). For linearization purposes, Bishop's parameter can be replaced by the effective saturation parameter (Lu *et al.*, 2010).

Based on equation (6) and the Mohr-Coulomb failure criteria (Fig. 1), LFS can be expressed as follows:

$$LFS = \frac{cos(\varphi').(c' + \sigma_{eff}{}^{I}.tan(\varphi'))}{\sigma_{eff}{}^{II}} \tag{8}$$

where $c'[kg.m^{-1}.s^{-2}]$ is the effective soil cohesion, $\varphi'[-]$ is the effective friction angle, the effective stresses $\sigma_{eff}{}^{I}[kg.m^{-1}.s^{-2}]$ and $\sigma_{eff}{}^{II}[kg.m^{-1}.s^{-2}]$ are the centre and the radius of the Mohr circle, respectively. $\sigma_{eff}{}^{I}$ and $\sigma_{eff}{}^{II}$ can be expressed in terms of the minor and major principal effective or total stress as follows (see Appendix A for more details):

$$\sigma_{eff}{}^{I} = \frac{\sigma_{eff}{}^{1} + \sigma_{eff}{}^{3}}{2} = \frac{\sigma^1 + \sigma^3}{2} - \chi\rho_w g h \tag{9}$$

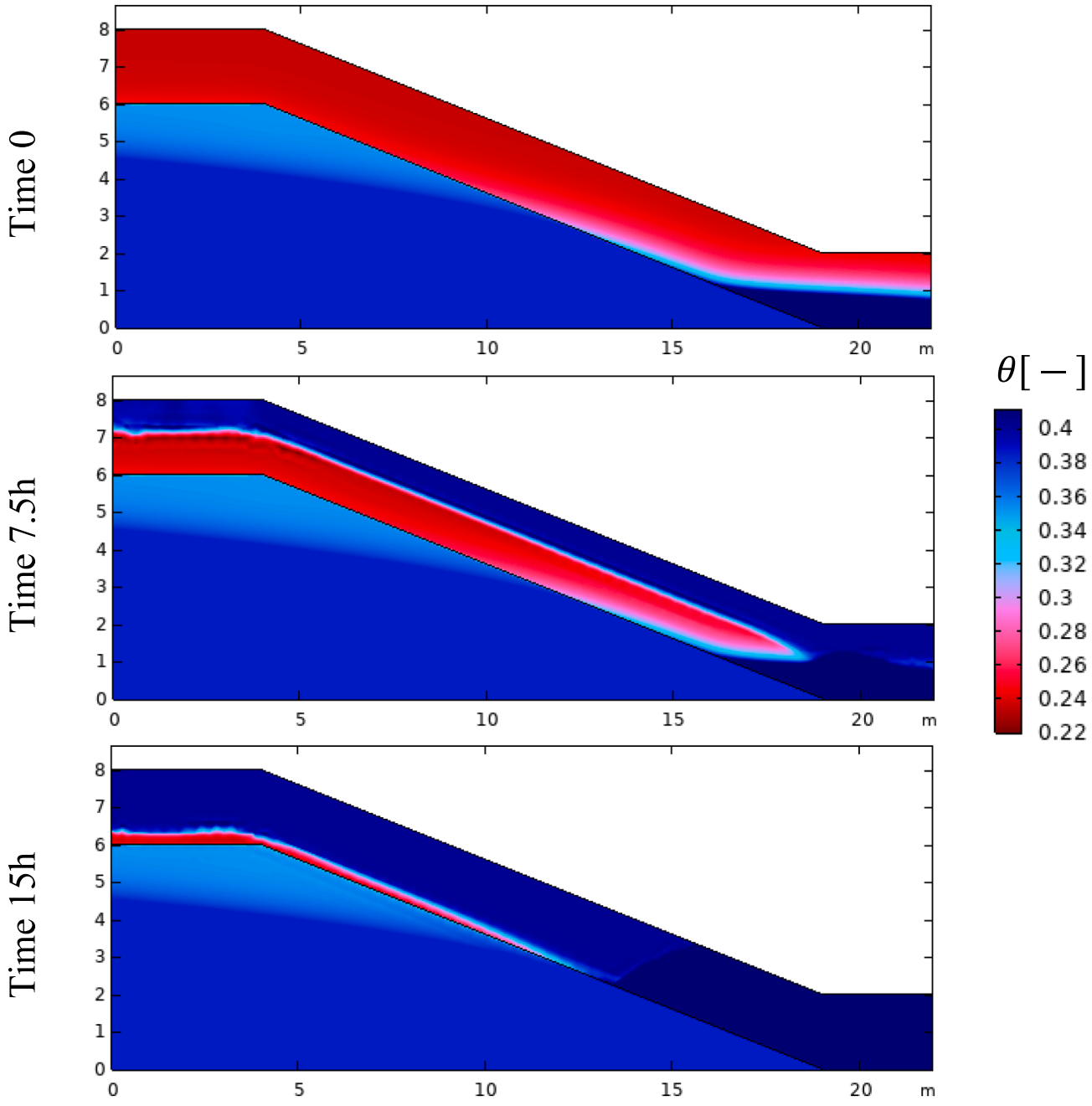


**Fig. 4.** Maps of water content at the equilibrium condition (top) and with high-intensity rainfall events at 7.5 h (middle) and 15 h (bottom).

$$\sigma_{eff}{}^{II} = \frac{\sigma_{eff}{}^{1} - \sigma_{eff}{}^{3}}{2} = \frac{\sigma^{1} - \sigma^{3}}{2} \tag{10}$$

where $\sigma_{eff}{}^{1}$ is major principal effective stress, $\sigma_{eff}{}^{3}$ is minor principal effective stress, $\sigma^{1}$ is major principal total stress, $\sigma^{3}$ is minor principal total stress.

### 2.3. Problem description: Geometry and boundary conditions

In order to carry out sensitivity analysis, we referred to a commonly used benchmark existing in previous studies (Moradi et al., 2018; Schilirò et al., 2015; Shao et al., 2015; Lanni et al., 2013; Lu et al., 2012). This hypothetical benchmark deals with rainfall on a hillslope. The domain extends over 42 m in length and 25 m in depth with a 23-degree slope in the middle (Fig. 2). A two-layered soil is considered to correspond to an upper layer of 2 m thickness along the topography overlaying the core lower layer. These layers have different hydrodynamic and mechanical properties. The simulations are performed for the whole domain; however, the risk of landslide is analyzed in an investigation area located in the middle. Considering the whole domain in the simulations allows for removing the impact of the boundary conditions on the model predictions. The top surface of the soil is assumed to be free of stress with imposed water flux corresponding to the rainfall. When soil becomes saturated, the top boundaries play the same role as seepage boundaries. Due to the increased runoff, the inclined surface of the soil receives a lower amount of water per surface unit than the horizontal surfaces. The normal rain flux on the slope is equal to the one on the horizontal surface, multiplied by the cosine of the inclination angle. The bottom and left boundaries are considered to be impermeable. The roller boundary condition (i.e. no normal displacement) is imposed on these

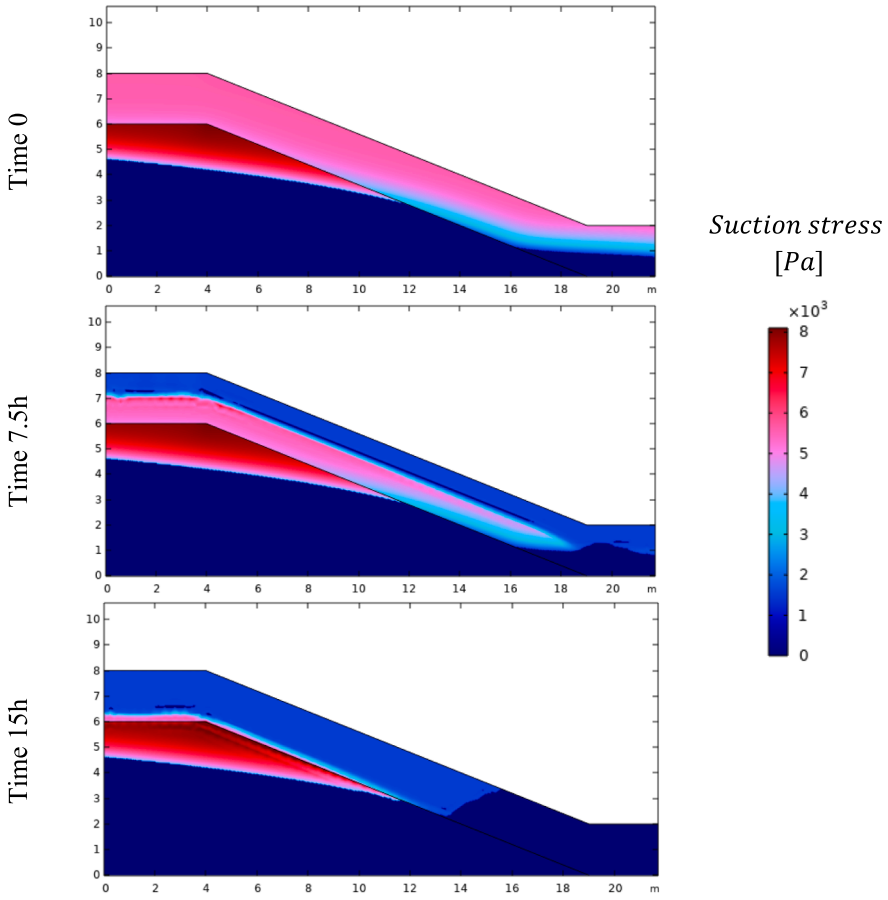


**Fig. 5.** Maps of soil suction at the equilibrium condition (top) and with high-intensity rainfall events at 7.5 h (middle) and 15 h (bottom).

walls. This boundary condition constrains the displacement in the normal direction of the surface, and imposes the absence of shear stress (no friction). The roller boundary condition is also imposed at the right surface, but a hydrostatic pressure head is imposed at the lower part of this surface and the seepage boundary condition is imposed at the top part. The seepage boundary condition assumes that the outflow is increasing with soil saturation.

The simulations are performed for 2 periods of rainfall. A first period of 10 years is simulated with a low-intensity rainfall of 600 mm/year, starting from hydrostatic pressure distribution as an initial condition, with a water table initially at position $z = 17\ m$. This period is simulated to predict the natural status of the soil. The results are used as initial conditions for the second period dealing with a high-intensity rainfall event (i.e., 20 mm per hour) during 15 h (Moradi et al., 2018; Shao et al., 2015).

The simulations are performed using a finite element model developed with COMSOL® Multiphysics by coupling the modules "Richards' Equation" and "Solid Mechanics" (Shao et al., 2014). The mesh is obtained in COMSOL with local refinement over the first 8 m of the soil.

## 3. a UA strategy for RILS

Uncertainty propagation analysis is performed to understand how uncertainties in model inputs can go through the model to reach the model outputs. To deal with a large number of uncertain parameters, we use an appropriate technique based on two sub-steps. The screening technique is first applied to eliminate insignificant parameters, followed by a GSA that allows for ranking the parameters by order of importance. This section presents the uncertain parameters, the model outputs, the screening technique and the GSA.

### 3.1. Uncertain parameters and quantities of interest

The hydrodynamics parameters of the upper and lower layers of soil are considered to be different, while the mechanical parameters are considered the same. This assumption is widely used for this benchmark in the literature (Lu & Likos, 2004; Lu & Griffiths, 2004). Thus, a total number of 14 parameters are considered uncertain in this study. This covers the hydrodynamic parameters of the upper and lower layers of soil, 5 parameters per layer (i.e. the parameters of the Brooks and Corey model), as well as the 4 mechanical parameters (i.e., Young's modulus, Poisson's ratio, soil cohesion, and the friction angle parameters). We investigate the sensitivity of selected quantities of interest to these parameters. The quantities of interest considered in the present analysis are designed to be relevant for the purpose of the study and to be dependent on the overall physical processes. The reliability of the sensitivity analysis depends also on the selected model outputs. For instance, it is well known that in some techniques of sensitivity analysis, such as with the screening technique, global metrics are more representative than local ones. We perform a preliminary analysis to select the quantities of interest relevant for RILS. Despite the fact that the primary variables of the model are the components of the displacement field, we select the LFS as the main metric because it is more relevant in investigating soil stability, which is the first goal of this work. As it will be discussed later in this paper, we show that the sensitivity analysis based on LFS provides reliable results. For the screening technique, we used two global metrics. The first one is the average $\overline{LFS}$ in the domain calculated over the investigation area. This is defined as follows:

$$\overline{LFS} = \frac{1}{|\Omega|}\iint_{\Omega} LFS \cdot d\Omega \tag{11}$$

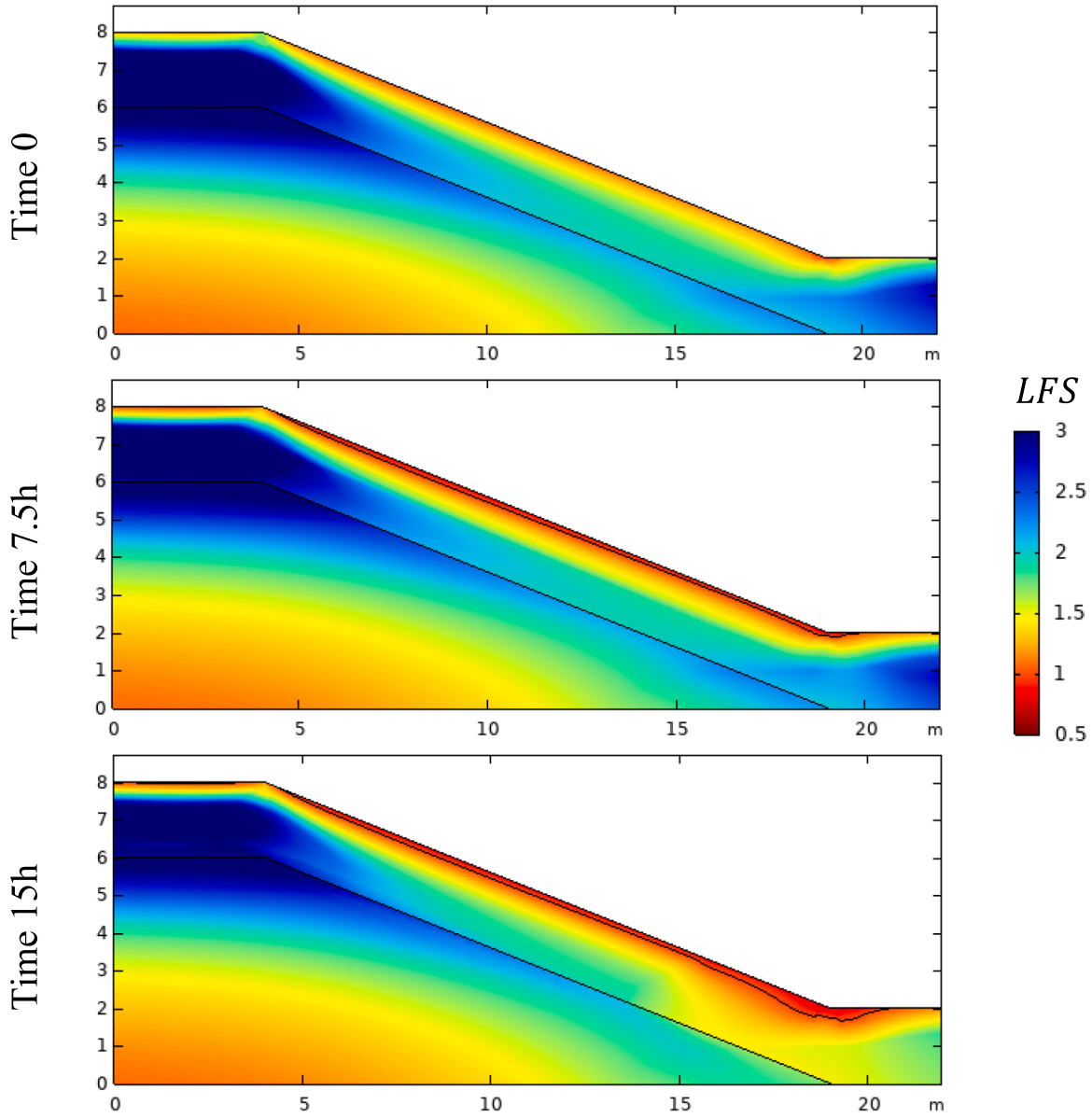


**Fig. 6.** Maps of LFS at the equilibrium condition (top) and with high-intensity rainfall events at 7.5 h (middle) and 15 h (bottom). The figure also shows a contour line of LFS equal to 1 at the top layer of the soil.

where Ω is the investigation zone and |Ω| is the area of this zone.

For a careful analysis of the soil stability, we also consider as output the area of the zone where LFS is less than one (i.e. area of the failure zone). The area of this zone can indicate the landslide susceptibility better than the average value of LFS over the domain. The more this zone is developed, the more the risk of landslides is significant. This is defined as follows:

$$A^{LFS} = \iint_{\Omega} LFS^{*} \cdot d\Omega \tag{12}$$

where Ω is the investigation area and $LFS^{*}$ is given by:

$$LFS^{*} = \begin{cases} 1 if LFS < 1 \\ 0 if LFS > 1 \end{cases} \tag{13}$$

As the processes are transient, we consider the values of these metrics at different observation times. However, in the results section, the analysis is performed with the outputs at the end of the first period and after 7.5 h and 15 h, respectively.

### 3.2. Screening technique

The screening technique aims to identify significant parameters and eliminate insignificant ones based on a reasonable number of runs. A specific design of experiments should be used in order to provide enough information on the model responses from an optimized number of simulations. In this study, we adopt the folded Plackett – Burman fractional factorial design (Wang et al., 2021). With this design, the number of runs is always a multiple of four. The corresponding design of experiments is based on the predetermined highest and lowest values of each parameter, over its range of variability. The general assumption is that interaction between more than two parameters can be neglected. A linear regression is applied to interpolate the model responses to the design of experiments. The coefficients of the regression function can then be used to calculate the standardized effect estimate which is usually represented in a Pareto chart (Vanaja & Shobha Rani, 2007). The

**Table 2**
The range for hydrodynamic and mechanical parameters of the soil layers for the analysis based on the screening technique.

| Symbol | Parameter | Units | High-level value | Low-level value |
|---|---|---|---|---|
| $\theta_s(u)$ | Saturated water content | – | 0.5 | 0.4 |
| $\theta_s(l)$ | *(u)*-upper layer *(l)*-lower layer | – | 0.39 | 0.2 |
| $\theta_r(u)$ | Residual water content | – | 0.05 | 0.01 |
| $\theta_r(l)$ | *(u)*-upper layer *(l)*-lower layer | – | 0.1 | 0.051 |
| $K_S(u)$ | Saturated hydraulic conductivity | cm/h | 3 | 1 |
| $K_S(l)$ | *(u)*-upper layer *(l)*-lower layer | cm/h | 0.1 | 0.01 |
| $\alpha_{BC}(u)$ | Brooks-Corey fitting parameters | 1/cm | 0.09 | 0.05 |
| $\alpha_{BC}(l)$ | *(u)*-upper layer *(l)*-lower layer | 1/cm | 0.04 | 0.01 |
| $n_{BC}(u)$ | | – | 0.4 | 0.2 |
| $n_{BC}(l)$ | | – | 0.19 | 0.1 |
| $E$ | Young's modulus | MPa | 12 | 8 |
| $\nu$ | Poisson's ratio | – | 0.4 | 0.2 |
| $\varphi'$ | Friction angle | ○ | 45 | 25 |
| $c'$ | Effective cohesion | kPa | 6 | 3 |

significance of a parameter can then be measured using the standardized effect estimate.

### 3.3. GSA: Variance-based technique and Sobol indices

Based on the screening technique, a certain number of insignificant parameters can be eliminated. The uncertainty with respect to the remaining significant parameters is performed with a GSA with the variance-bases technique and the Sobol indices. GSA allows for quantifying the combinations of input parameters that mostly contribute to the variability of the model outputs. This allows for an understanding of how uncertainty in the output variables is affected by uncertainties in the model inputs (Saltelli et al. 2008; Razavi & Gupta, 2016; Homma & Saltelli, 1996). This technique has been widely used for applications involving flow and transport processes in soil (Rajabi et al., 2020 and references therein). For the measurement of the sensitivity, we used the Sobol indices (Sobol', 1993). These indices do not assume linear or monotonous variation of the forward models (Fajraoui et al., 2017) and they can be easily interpreted. The first-order Sobol index can measure the sensitivity of an output to a given parameter, without considering interaction with other parameters. It expresses the ratio between the variance of an output with respect to the selected parameter to the total variance involving all parameters. The total contribution of an input parameter to a model output that takes into account the interaction with other parameters can be measured with the total Sobol indices (Fajraoui et al., 2017).

### 3.4. Surrogate modeling: PCE

Sobol indices can be evaluated with the Monte Carlo method. This technique requires a huge number of runs of the physical model. It is impractical from a computational point of view, especially when the forward model is highly consuming in computational resources. A surrogate model can be used to reduce the computational costs of evaluation of Sobol indices. The surrogate model can be obtained based on a reduced number of runs of the physical model (Zhang et al., 2023; Zheng et al., 2023). It is then used to evaluate the Sobol indices. Different techniques of surrogate modeling exist in the literature (Asher et al., 2015). Among these techniques, we used the technique of PCEs that approximates the model outputs as a polynomial function of the input parameters. PCE is selected because the Sobol indices can be analytically expressed in terms of the PCE coefficients (Fajraoui et al., 2017). Thus, in this work, hundreds of runs are performed. A major part of the data is used for building the PCE via a regression problem. The rest of the data is used for checking the PCE. The sparse technique for calculating PCE, proposed by Shao et al. (2017), is used in this work. This technique allows for eliminating the insignificant polynomial coefficients and in consequence providing high accuracy with a reduced number of regression coefficients. In-house codes have been used for obtaining the PCE and evaluating the Sobol indices. The workflow of our analysis is depicted in Fig. 3.

## 4. Results and Discussions

### 4.1. Verification of the numerical model

Verification of the developed COMSOL® model is a pre-requirement before uncertainty analysis. The verification is investigated using the benchmark described in the previous sections and by comparing the COMSOL® model to results published in previous studies. All the parameters used in the simulations are considered to be the same as in Shao et al. (2015). The parameters are summarized in Table 1. A mesh of about 3 K nodes is used in the simulations. This mesh is obtained by using extremely fine mesh for the first 8 m of the soil and normal mesh for the layer below 8 m.

The flow model is assessed with the spatial distributions of the water content at different time steps. The results are depicted in Fig. 4. At the end of the equilibrium period (i.e. steady state), the upper layer of the soil is partially saturated. After 7.5 h of high-intensity rainfall, the top part of this layer becomes saturated due to water infiltration. As the permeability of the top layer is higher than the lower one, the top layer is the preferential flow path of groundwater. It is then accumulated downstream below the horizontal surface, where a zone of high saturation, almost saturated, can be observed. After 15 h of high-intensity rainfall, the upper layer of soil becomes almost saturated. The relative permeability of this zone increases. This zone becomes the preferential pathway flow for infiltrated water. This is why, as observed in Fig. 4, the zone below the top surface of the bottom layer of soil remains partially unsaturated. The results depicted in Fig. 4 shows perfect agreement with the results in Shao et al. (2015), which validates the model.

Fig. 5 shows the variation of the suction stress in the domain which is defined by $\chi\rho_w g|h|$ when $h$ is negative (i.e. above the water table) and zero when $h$ is positive (i.e. below the water table). At the initial equilibrium the suction stress is more important in layer 2 than layer 1. During the rainfall even, the suction stress in decreasing due to water infiltration in the domain.

The mechanical model is assessed with the maps of LFS. The maps are presented in Fig. 6. This figure shows that at the end of the equilibrium period, the zone where LFS is less than one (i.e. the failure-prone zone) is contracted to the top surface, indicating that there is no risk of landslide at this condition. After 7.5 h of high-intensity rainfall, and due to the increase of water saturation in the top layer of soil, the failure-prone zone grows in a homogeneous way below the slope due to water infiltration. After 15 h of intensive rainfall, the failure-prone zone is still growing but it becomes more developed around the bottom part of the slope. This can be attributed to the high fluid pressure in this zone related to water accumulation as shown in Fig. 4. This figure allows for predicting the zone where the failure will initiate. The LFS maps also show a perfect agreement with Shao et al. (2015).

### 4.2. Results of the screening technique

We perform the UA for this hypothetical benchmark to evaluate the performance of the strategy proposed in this work. For the sensitivity analysis, we assume that both layers of soil have the same mechanical properties. Thus, 14 parameters are assumed to be uncertain. These parameters and their ranges of variability are defined in Table 2. We assume that no prior knowledge about the soil is available. The ranges

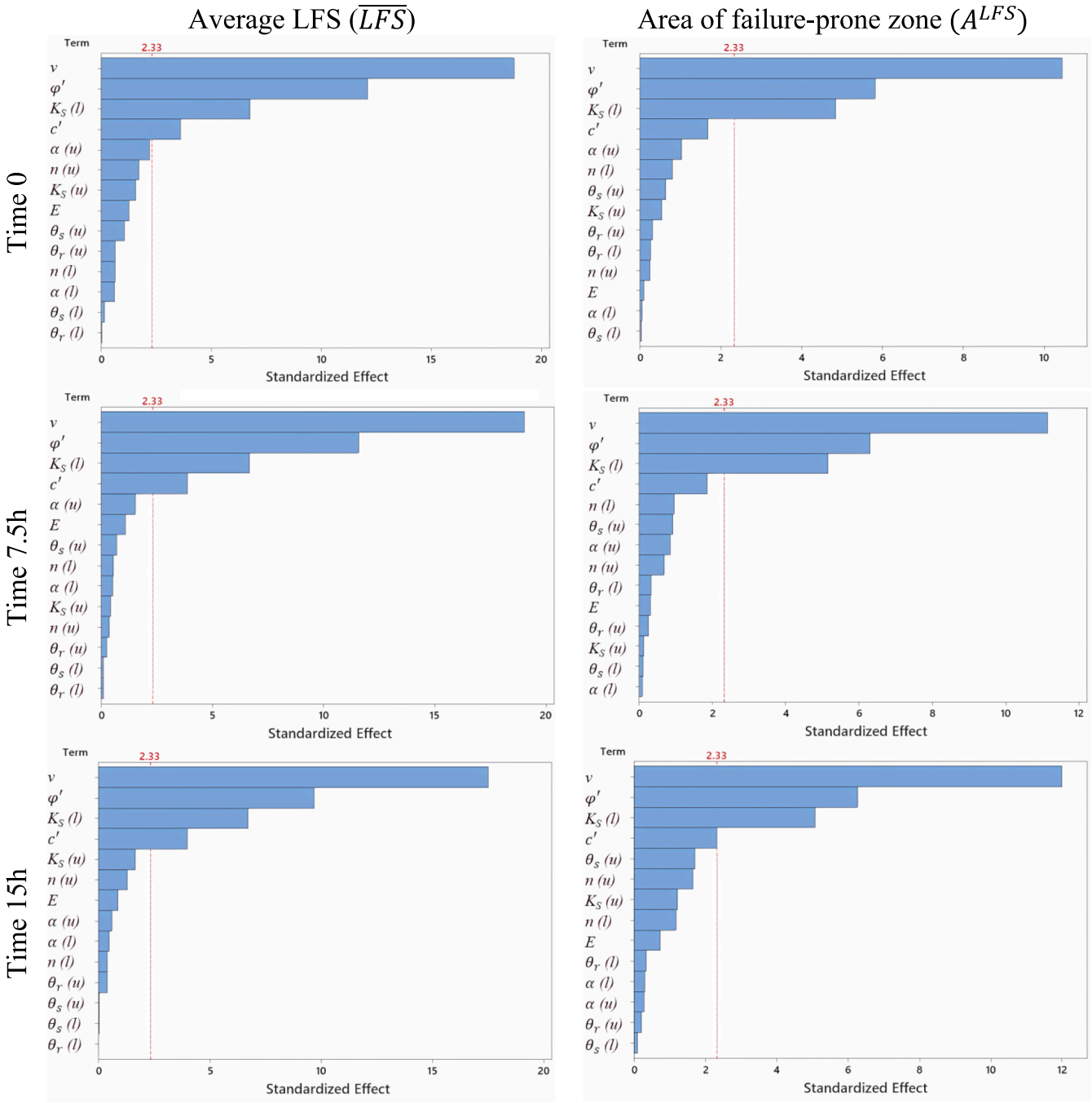


**Fig. 7.** Pareto Chart representing the standardized effects of parameters on the average LFS and the area of failure-prone zone at different time outputs.

under consideration are based on Shao et al. (2015) and defined by a trial and error procedure in order to ensure the significance of the model outputs. Dry unit weight of the solid grains is kept constant as in Table 1.

A simplified Plackett – Burman design of experiments is used to identify which factors significantly affect the model output. The number of factors is considered to be N = 14, which corresponds to a design of experiments with 36 sets of parameters. Both $\overline{LFS}$ and $A^{LFS}$ (equations (11) and (12) are considered as model outputs.

The Pareto Chart representing the standardized effect of parameters on $\overline{LFS}$ and $A^{LFS}$ with the 97 % confidence levels are given in Fig. 7, for different time outputs. The figure shows the statistically significant parameters placed at a higher than the significance limit of 0.3 corresponding to a standardized effect greater than 2.33. The effective soil cohesion ($c'$), effective friction angle ($\varphi'$), Poisson's ratio ($\nu$) and saturated hydraulic conductivity of the lower layer of soil ($K_S(l)$) are the most influencing parameters on $\overline{LFS}$. The results are the same for all time steps. The hydraulic conductivity $K_S(l)$ controls the infiltration of water to the lower layer of soil. This infiltration plays a major role on the flow in the upper layer and impacts the stress distribution. For instance, when $K_S(l)$ is low, the infiltration of water to the lower layer is very weak. As a consequence, water storage in the upper layer is high and the related stress is important. This increases the risk of landslide. The Poisson coefficient ($\nu$) influences soil stability because it controls the ratio between the lateral and axial strains. The largest stress principal axis is close to vertical direction in the initial situation because it is related to the weight of the soil and stored water. Thus, the axial strain is vertical and the lateral strain is horizontal. Consequently, sliding is mainly related to lateral strain. The uncertainty on effective soil cohesion ($c'$) and effective

**Table 3**
The parameters considered in the GSA and their range of variability.

| | Parameter | Units | High-level value | Low-level value |
|---|---|---|---|---|
| Uncertain parameters | $K_S(l)$ | cm/h | 0.1 | 0.01 |
| | $\nu$ | – | 0.4 | 0.2 |
| | $\varphi'$ | ○ | 45 | 25 |
| | $c'$ | kPa | 6 | 3 |
| | Parameter | Units | Value | |
| Deterministic parameters | $\theta_s(u)$ | – | 0.412 | |
| | $\theta_s(l)$ | – | 0.385 | |
| | $\theta_r(u)$ | – | 0.041 | |
| | $\theta_r(l)$ | – | 0.09 | |
| | $K_S(u)$ | cm/h | 2.59 | |
| | $\alpha_{BC}(u)$ | 1/cm | 0.068 | |
| | $\alpha_{BC}(l)$ | 1/cm | 0.027 | |
| | $n_{BC}(u)$ | – | 0.322 | |
| | $n_{BC}(l)$ | – | 0.131 | |
| | $E$ | MPa | 10 | |

friction angle ($\varphi'$) influences the critical shear strength ($\tau^*$). Regarding $A^{LFS}$, the same parameters as $\overline{LFS}$ appear to be significant, except the effective soil cohesion ($c'$). The fact that almost identical significant parameters are obtained for $\overline{LFS}$ and $A^{LFS}$ and that this holds for all time steps gives confidence to the outputs chosen in our analysis. It indicates that both metrics $\overline{LFS}$ and $A^{LFS}$ are suitable for performing UA for RILS. Based on the results of the screening technique, the most significant parameters (i.e., $\varphi', c', K_S(l)$ and $\nu$) will be then used in the GSA that aims at ranking these parameters while considering the interactions between them.

It is relevant to note that the results of the screening technique are in general coherent with the analysis based on the global factor of safety. This further indicates that when the slope infinite assumption is valid, the global factor of safety can be expressed as a function of $\varphi'$, $c'$ and the water pressure (Baum et al., 2010) (see Appendix A). For $\varphi'$ and $c'$, this is fully coherent with the results of our analysis. Regarding $K_S(l)$ and water pressure, the results are also coherent because $K_S(l)$ controls the water infiltration to the lower layer of soil and, in consequence, water pressure is directly related to $K_S(l)$. This coherence with the approach based on the global factor of safety gives additional confidence to our analysis. However, unlike the global factor of safety, our analysis shows that the Poisson coefficient has a significant role on slope stability. But this dependency on the Poisson ratio is coherent with the results of the concept of the general factor of safety based when the slope is assumed to be finite and slope depth is considered as infinite (see Appendix A). Under these assumptions and when there are no tectonic stresses and no external load, the factor of safety is only a function of Poisson ratio and friction angle (Moradi et al., 2018).

The results of the sensitivity analysis are specific to the investigated test case and ranges of variability of the uncertain parameters. The results could be different for other configurations. For example, when we reduce the range of variation of the Poisson's ratio to 0.1 (from 0.3 and 0.4), Poisson's ratio is no longer the most important parameter. It becomes the second most important parameter. The sensitivity of the LFS to Poisson's ratio decreases also when the horizontal size of the domain is increased. This is consistent with the results of the infinite slope analysis, for which the analytical LFS is independent of Poisson's ratio.

### 4.3. Building and verifying the PCEs

As explained previously a surrogate model based on the PCEs is used for performing the GSA. To construct PCEs, we first generate data by assuming 4 uncertain parameters. The parameters and their range of variability are summarized in Table 3. All other parameters as assumed to be constant, with corresponding values given in Table 3. The density of the solid grains is kept constant as in Table 1. The data are generated by assuming that the parameters are uniformly distributed over the ranges of variability and using a design of experiments assembling 200 samples. These samples are generated via random technique with the Latin hypercube sampling approach, a common statistical method for sampling. This approach divides the given range of parameters into equidistant intervals. Then it selects one random value from each interval. As in the screening technique analysis, $\overline{LFS}$ and $A^{LFS}$ are considered as outputs. Moreover, due to its flexibility, GSA is also used to investigate the space variability of the uncertainties. This obtained by providing spatial maps of the Sobol indices. To manage the time dependency, we use three selected time outputs at the end of the equilibrium period and after 7.5 h and 15 h of high-intensity rainfall. The CPU time for data generation is about 4 days. We run the simulation on a computer system with an Intel@544CoreTM i7-6700 CPU at 3.4 GHz and with 16 GB of RAM. The CPU times for the different set of parameters are not the same. It can range from few minutes for certain sets to more than 3 h for others. The most consuming samples are when the hydraulic conductivity of the upper layer of soil is lower than the rainfall intensity. The PCEs are built by assuming the third polynomial order and by using the sparse technique developed by Shao et al. (2017). This technique allows for optimizing the number of samples required for obtaining accurate results by excluding insignificant terms from the PCEs. We use in-house codes to build the sparse PCEs and to evaluate the

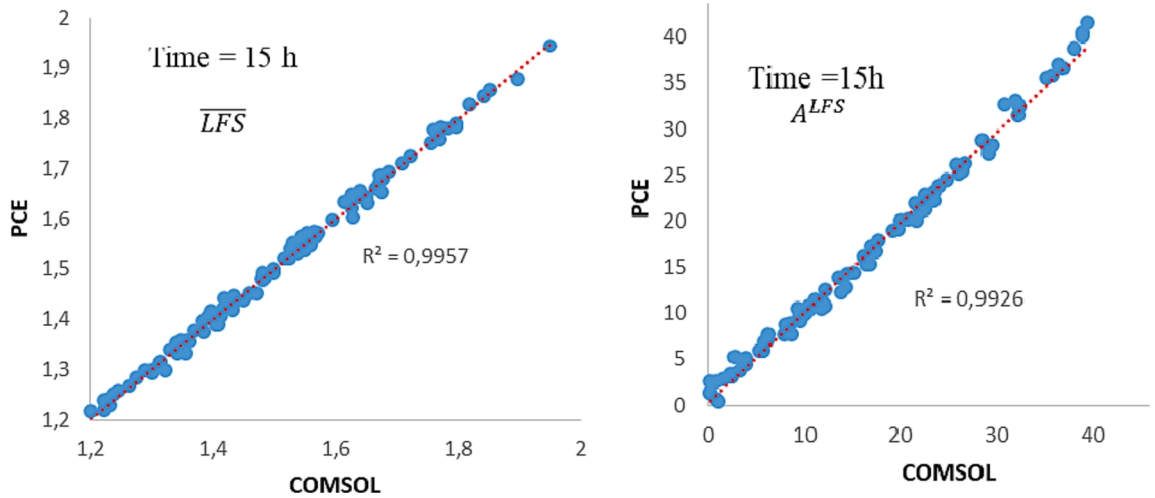


**Fig. 8.** Validation of PCE: Comparison between PCE and the initial COMSOL® model for the $\overline{LFS}[-]$ (at left) and $A^{LFS}[m^2]$ (at right).

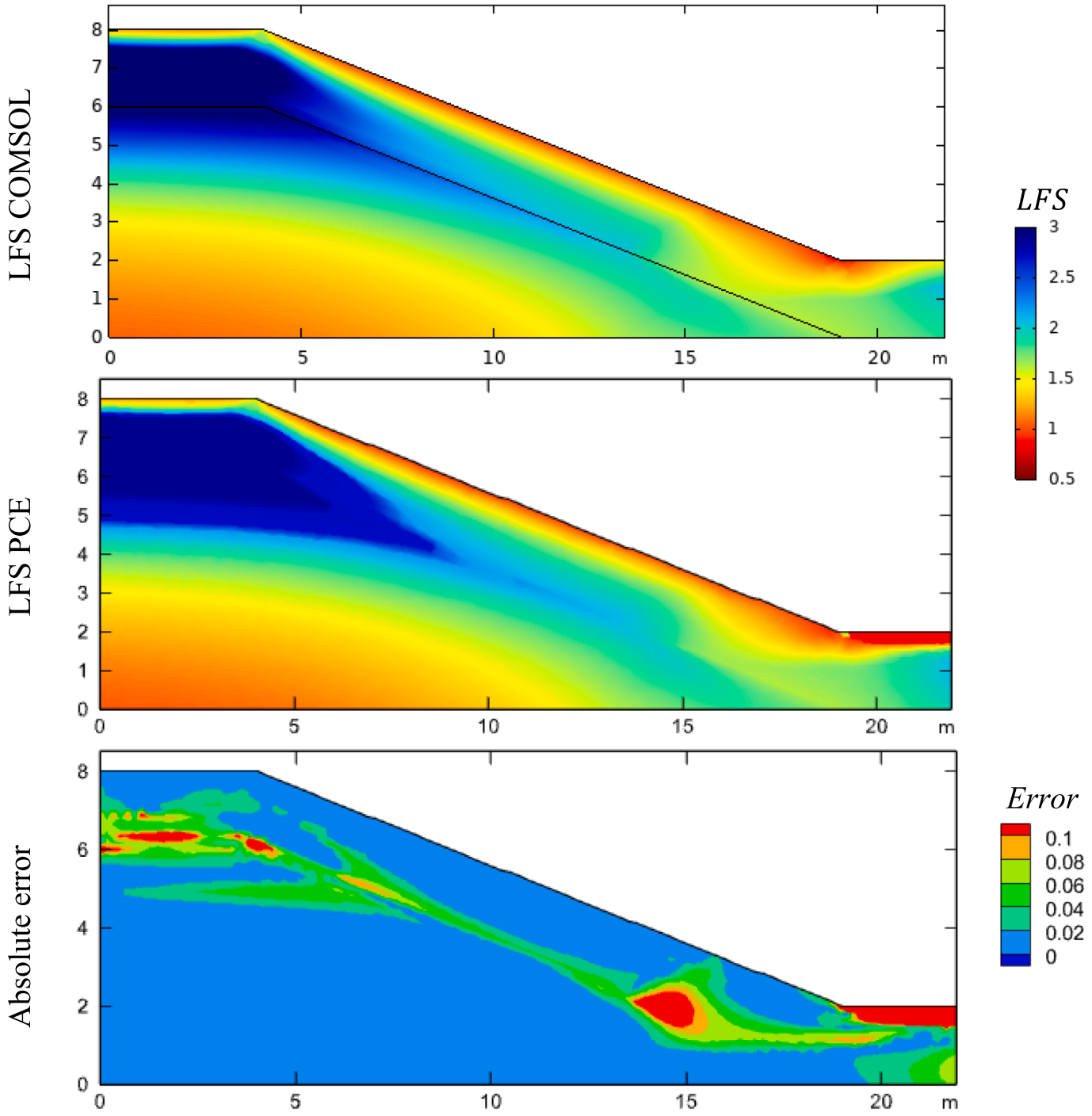


**Fig. 9.** Comparison between the values LFS maps obtained with COMSOL® (top) and PCE (middle) and corresponding absolute error (bottom). Results presented after 15 h of high-intensity rainfall for $K_s(l) = 0.06cm/h; \nu = 0.35; \varphi' = 35^{\circ}; c' = 5kPa$ (other parameters are kept as in Table 3).

Sobol indices.

the accuracy of the PCEs IS investigated to give confidence to the resulting GSA. To do so, once the PCEs have been built, we use 100 new samples to compare the results of the constructed PCEs with the results of the initial mode. A sample of the comparison results is depicted in Fig. 8. This figure compares the results of PCEs and COMSOL® at the end of the simulation. We can observe a pretty good match in this validation stage with high percentage of the "R-square". Verification is performed for different time outputs, but results are presented only for t = 15 h. We should mention that the values of $\overline{LFS}$ for all the samples are greater than one. This cannot indicate that there is no risk of landslide; In general, the smaller is $\overline{LFS}$, the higher is the risk of failure. $A^{LFS}$ can be more suitable for quantitatively evaluating the risk of landslide. When $A^{LFS}$ is zero, there is no local value of LFS less than one, thus there is no risk of failure. If $A^{LFS}$ is higher than zero, there is a risk of failure in some zone, and this risk is more important for high values of $A^{LFS}$.

We also verified the accuracy of the LFS maps predicted by the PCEs by comparing them to the ones obtained with the physics-based model (COMSOL®). Constructed PCEs are based on nodal (3199 nodes) values of LFS. An example of such a comparison is represented in Fig. 9. The results are obtained for $(K_s(l) = 0.06cm/h; \nu = 0.35; \varphi' = 35^{\circ}; c' = 5kPa)$. Other parameters are kept as in Table 3. Fig. 9 provides the map of the

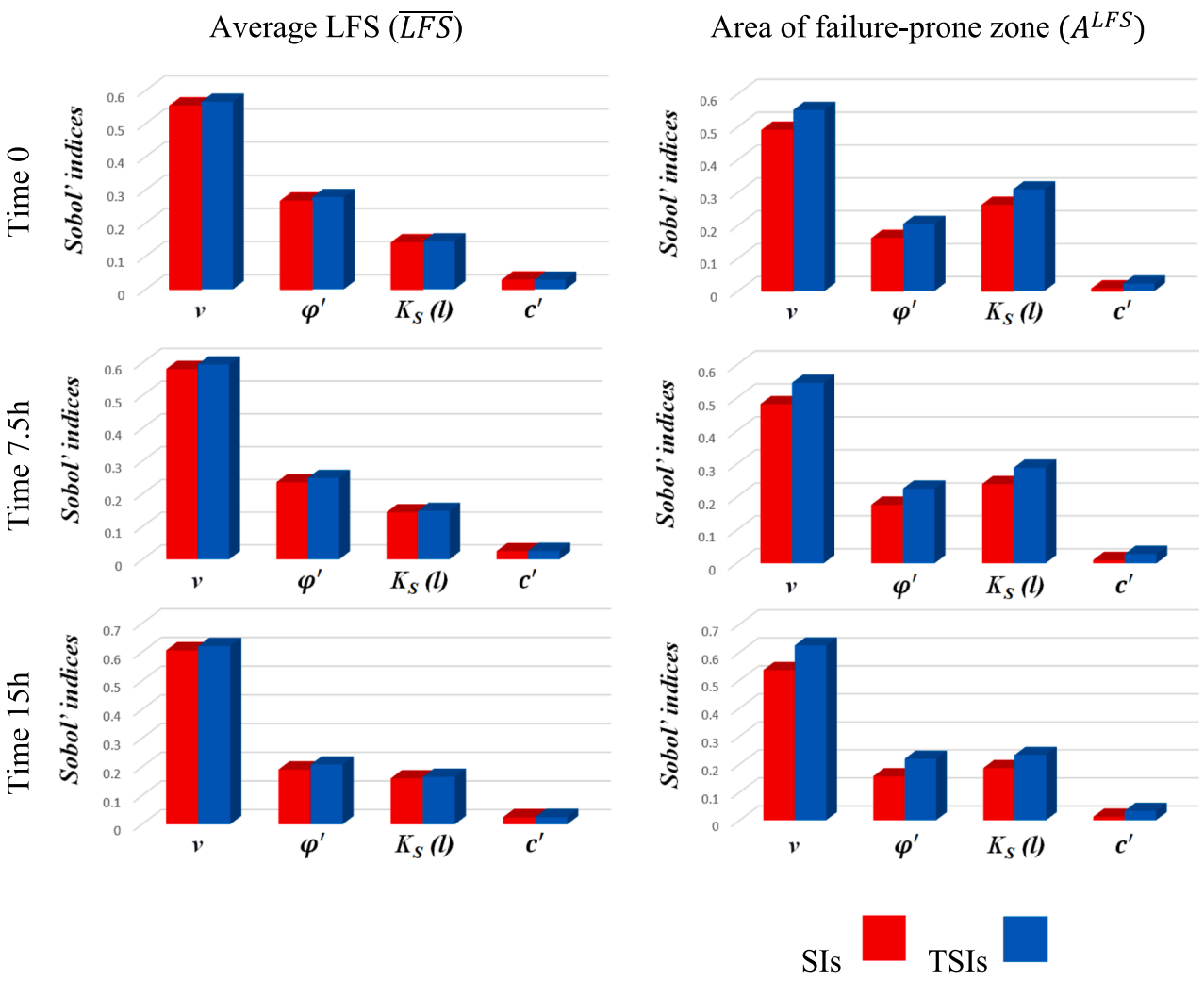


**Fig. 10.** First-order (in red) and total (in bleu) Sobol indices indicating the sensitivity of $\overline{LFS}$ (at left) and $A^{LFS}$ (at right) to $K_s(l), \nu, \varphi'$ and $c'$ at different time outputs.

discrepancy between COMSOL® and PCE. It allows for quantifying and localizing the deviations between the initial model and the surrogate one. The discrepancies are very small, which demonstrates an excellent match between the outputs of COMSOL and PCE. The average error is calculated to be 0.047. The highest error is observed at the interface between the upper and lower layer of soil and close to the lower horizontal surface.

### 4.4. Results of the Sobol Indices: Ranking the parameters by order of importance

Fig. 10 represents the sensitivity of the model's outputs ($\overline{LFS}$ and $A^{LFS}$) to the uncertain inputs. The figure depicts the bar plots of the first-order and the total Sobol indices at different time outputs (i.e. 0 h, 7.5 h, and 15 h). These indices allow for ranking the parameters by order of significance. It is clear that for the three time outputs under consideration, the Poisson coefficient is the most significant parameter, for the observed time outputs. As explained above, Poisson coefficient plays an important role in controlling transverse deformations which are the main causes of sliding.

For the observed time outputs, the friction angle ($\varphi'$) is the second parameter contributing to the uncertainty on $\overline{LFS}$, followed by the hydraulic permeability of the lower layer of soil ($K_s(l)$). The angle of friction $\varphi'$ controls the limit of the Mohr-Coulomb criterion, while $K_s(l)$ plays a major role in the water infiltration to the lower layer in soil and, in consequence on the amount of water stored in the upper layer of soil and the related groundwater flow below the slope. The order of these parameters is inversed for $A^{LFS}$ as the uncertainty on this metric is more related to the uncertainty on $K_s(l)$ than $\varphi'$ for the first time steps (0 h and 7.5 h). An equivalent sensitivity of $A^{LFS}$ to these parameters is observed at the last time output (15 h). As $A^{LFS}$ covers the zone at the upper layer of soil where the shear stress ($\tau$) is close to the shear strength ($\tau^*$) (i.e. LFS is quite small), it seems normal that it is more sensitive to the parameter controlling the gravitational load forces (i.e. weight of water) than the one controlling the critical shear strength ($\tau^*$). With time, the failure-prone zone expands in depth and covers areas where LFS is quite close to one. In this case, the sensitivity to $\varphi'$ becomes more significant. As $A^{LFS}$ is more relevant for measuring the risk of landslide than $\overline{LFS}$, the main conclusion here is that uncertainty on the prediction of landslide susceptibility is more related to $K_s(l)$ than $\varphi'$ for the first periods of rainfall. The sensitivity to $\varphi'$ increases with time, while the sensitivity to $K_s(l)$ decreases. Fig. 10 shows that the effective cohesion coefficient ($c'$) is ranked last with slight effect on the both $\overline{LFS}$ and $A^{LFS}$ .

We should notice that the resulting parameters' ranking is coherent with the concept of global factor of safety under the assumption of infinite slope. The sensitivity of the global factor of safety to these parameters can be evaluated using the partial derivatives. The results show that the derivative with respect to $\varphi'$ is two orders of magnitude higher than the derivative with respect to $c'$. The same analysis can also be performed with the factor of safety that can be obtained with the

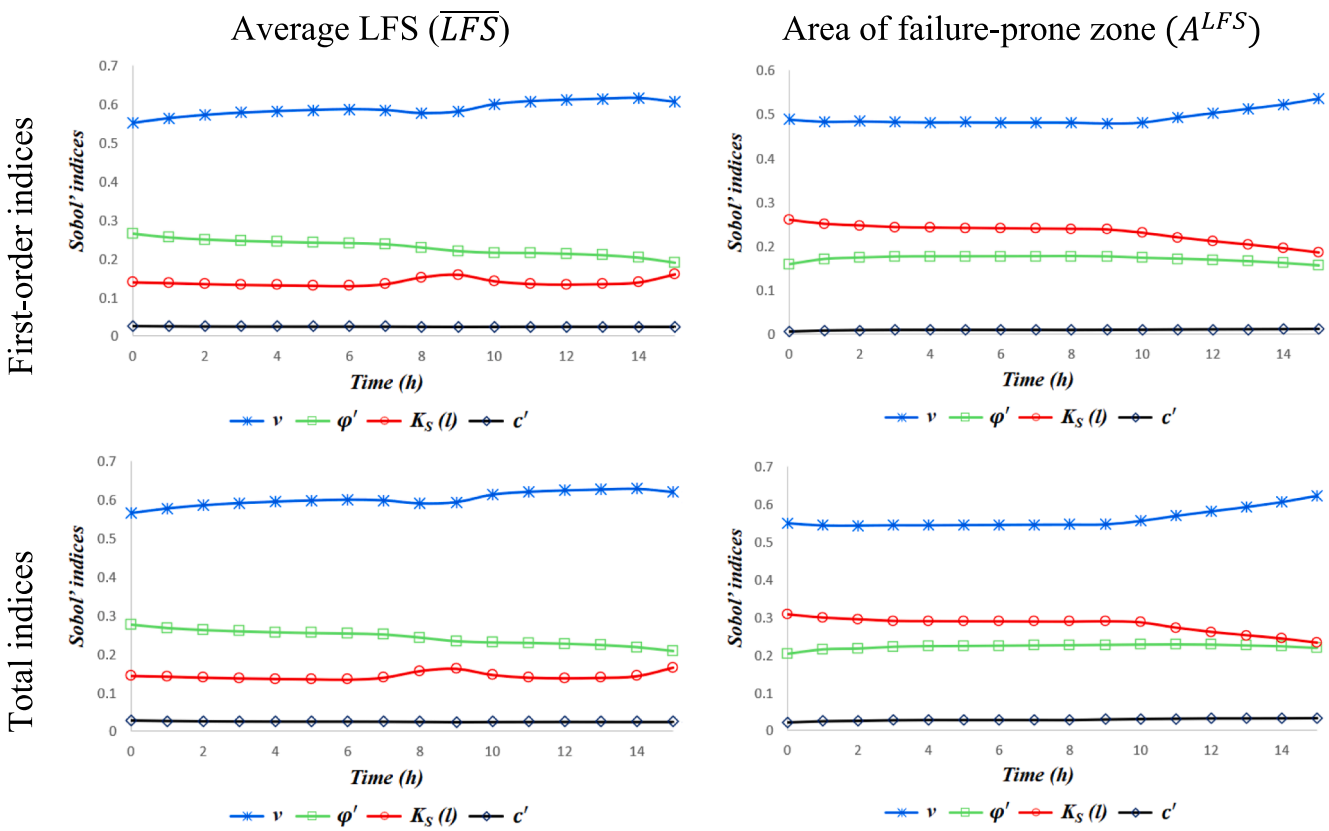


**Fig. 11.** Time variations of the first-order Sobol indices (top) and total Sobol indices (bottom) for $\overline{LFS}$ (left) and $A^{LFS}$ (right).

assumption of infinite depth and no external load. In this case, the factor of safety can be expressed as a function of the $\nu$ and $\varphi'$. The results show that the derivative with respect to $\nu$ is one order of magnitude higher than that for $\varphi'$, which is in full agreement with the results of the GSA.

It is also important to note that first-order and total Sobol indices are almost equivalent, as shown in Fig. 10. This indicates that the interaction between parameters is insignificant. This point can explain why the ranking obtained with the screening technique is almost equivalent to the one resulting from the GSA.

In order to investigate the sensitivity of $\overline{LFS}$ and $A^{LFS}$ to the parameters overall the period of intensive rain-fall, we plot in Fig. 11 the time variation of the total Sobol indices. Fig. 11 confirms that the ranking of parameters, observed in Fig. 10, is valid overall the rainfall period. It is clear that the sensitivities to $c'$ and $\nu$ are independent on time for both $\overline{LFS}$ and $A^{LFS}$. The Sobol indices of $\overline{LFS}$ and $A^{LFS}$ with respect to $\varphi'$ and $K_s(l)$ are slightly time-dependent. For $\overline{LFS}$, the Sobol indices with respect to $\varphi'$ (resp. $K_s(l)$) is decreasing (resp. increasing) with time. An opposite trend of variations are observed for $A^{LFS}$.

In order to investigate the spatial variability of the sensitivity coefficients, we plot in Fig. 12 the spatial maps of the total Sobol indices at the end of the intensive rainfall period. This analysis is important to investigate the effect of uncertainties in the model inputs on the location of the zone where the landslide could initiate. We limit the discussion to total Sobol indices, because first-order and total Sobol indices are almost equivalent. At first look, the scales in Fig. 12 confirm the ranking observed in Figs. 10 and 11. The highest values of total Sobol indices with respect to $\nu, \varphi', K_s(l)$ and $c'$ are 0.95, 0.8, 0.65, and 0.55, respectively. The map of standard deviation shows high variability of LFS in zones far from the slope. The high variability in this zone is insignificant when regarding the landslide susceptibility because the values of LFS are high (see Figs. 6 and 9) and there is no risk of landslide in this zone. Below the slope the variability is weak, but knowing that the values of LFS are small in this zone, this variability is important for landslide susceptibility. Two zones where high sensitivity to $\nu$ can be observed. The first one is located at the top of the domain, relatively far from the slope, while the second one is close to the slope's bottom part. Thus, the latter is important for the landslide susceptibility. This result indicates that the Poisson ratio has a major role in controlling the location where the failure initiates. The zone of high sensitivity to $\varphi'$ is located directly below the slope. This is why its sensitivity to $\varphi'$ is very important for landslide susceptibility. Complementary results can be observed between $\nu$ and $\varphi'$. High sensitivity to $K_s(l)$ can be observed at the left part of the domain, but most significantly the zone of relatively high sensitivity close to the bottom part of the slope is relevant for landslide susceptibility. The zone of high sensitivity to $K_s(l)$ is close to the slope bottom part. This $K_s(l)$ plays an important role in controlling the location of the landslide rupture surface. Sensitivity to $c'$ is relatively low, but it is located in the area where there is a high risk of landslide.

### 4.5. Marginal effects

The comparison between total and first-order Sobol indices shows that the interaction between parameters is slightly significant. This allows for investigating the marginal effect of the significant parameters on the model outputs. The marginal effect of a parameter, also denoted as invariant effect, corresponds to the effect of a parameter of its range of uncertainty while all other parameters are kept invariable at their average values. The marginal effect can be calculated using the surrogate PCE model. We investigate the marginal effect of the significant parameters (i.e., $\nu, \varphi', K_s(l)$ and $c'$) on $\overline{LFS}$ and $A^{LFS}$. The results are given in Fig. 13. This figure show the variation of the outputs with respect to $\nu$. This parameter has an increasing effect on $\overline{LFS}$ and decreasing effect on $A^{LFS}$. Both figures indicate that there is less risk of landslide when the

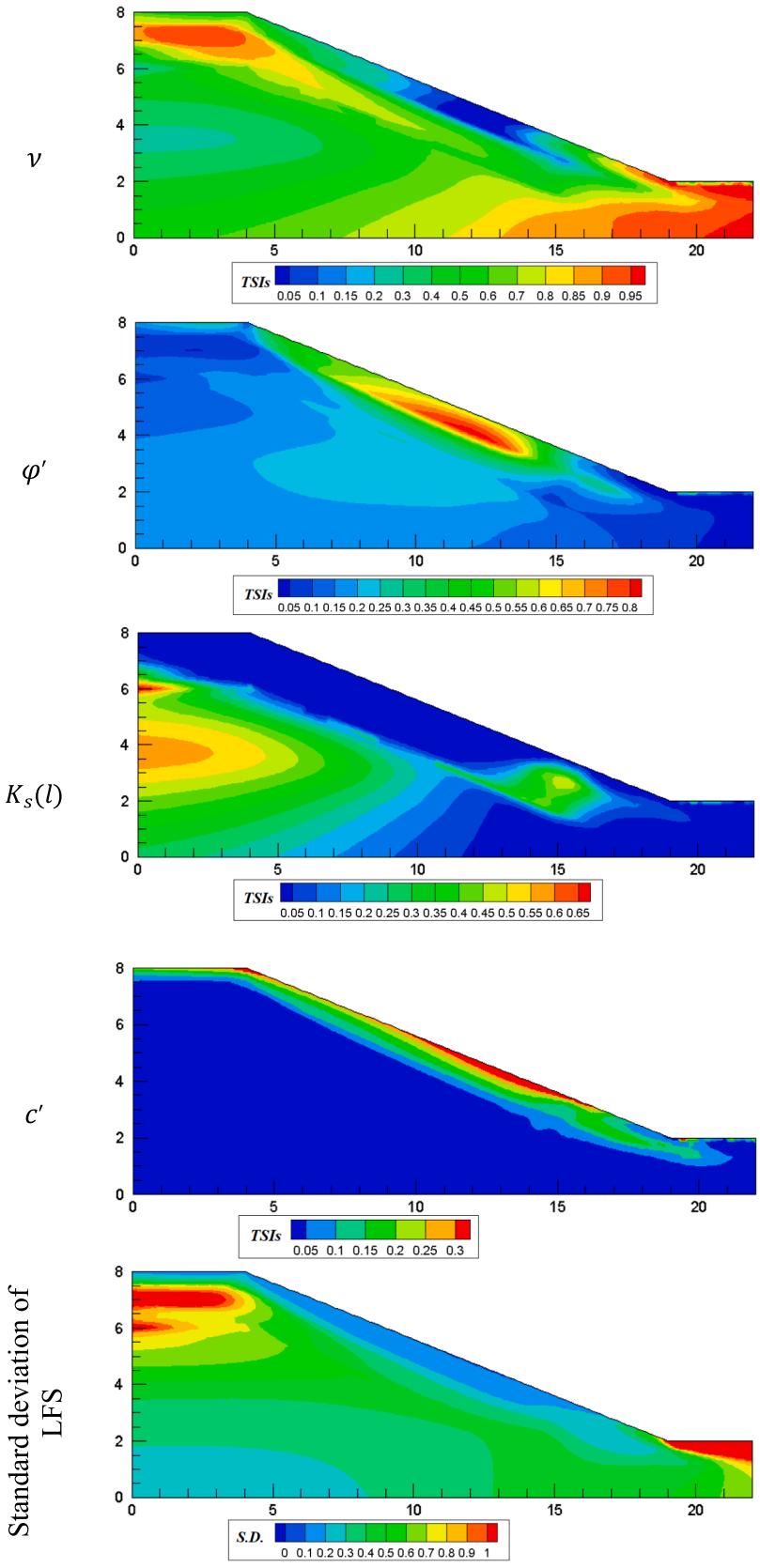


**Fig. 12.** Spatial distribution of the total Sobol indices and the standard deviation of LFS after 15 h of high-intensive rainfall.

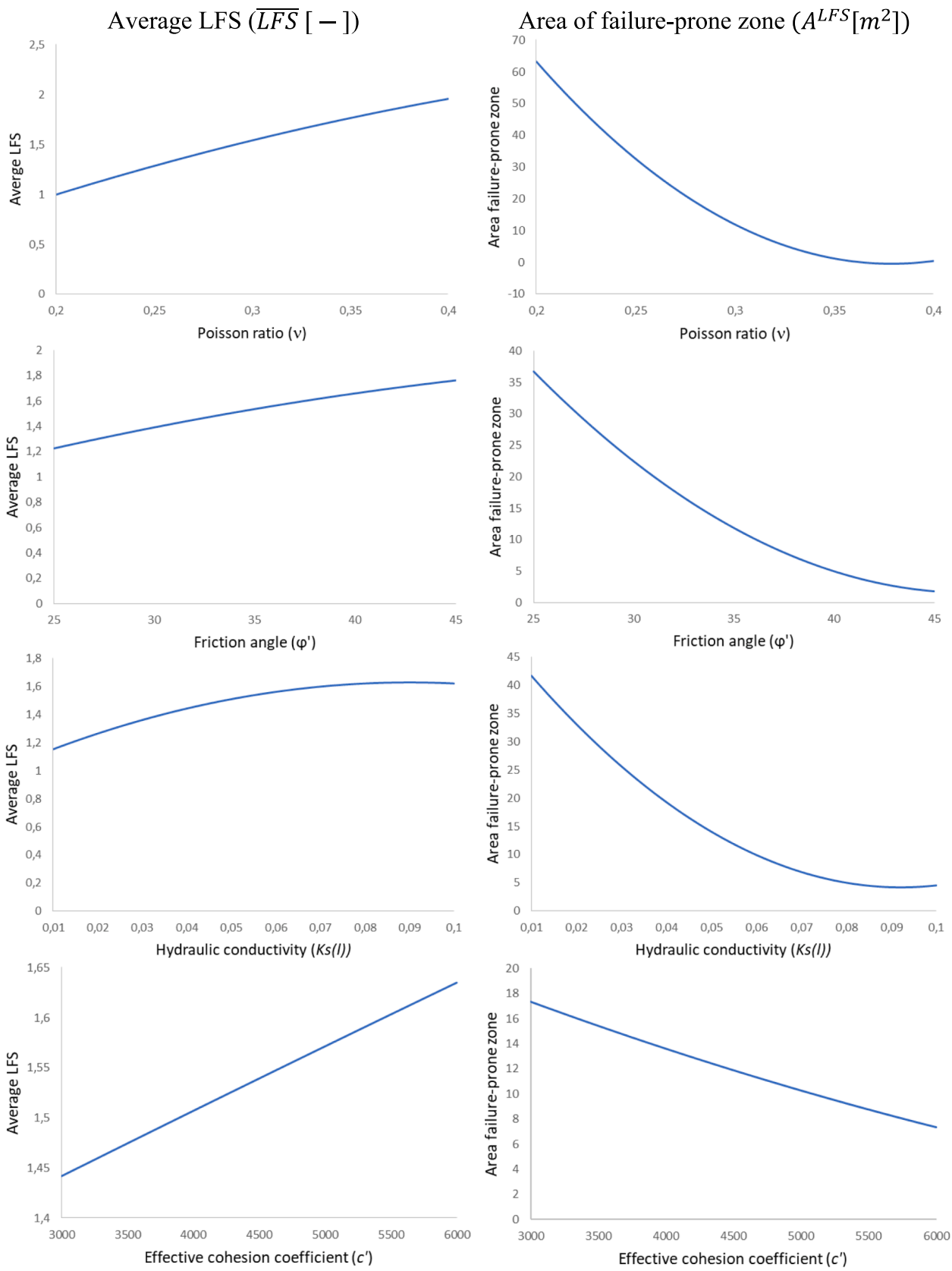


**Fig. 13.** Marginal effects of the main significant parameters (i.e., $\nu, \varphi', K_s(l)$ and $c'$) on $\overline{LFS}$ and $A^{LFS}$.

**Table 4**
Ranges of the parameters used for the uncertainty quantification analysis.

| Parameter | Units | Deterministic value | Uncertainty | Low-level value | High-level value |
|---|---|---|---|---|---|
| $K_S(l)$ | cm/h | 0.05 | 10 % | 0.045 | 0.055 |
| $\nu$ | – | 0.3 | 10 % | 0.27 | 0.33 |
| $\varphi'$ | ○ | 35 | 10 % | 31.5 | 38.5 |
| $c'$ | kPa | 4.5 | 10 % | 4.05 | 4.95 |

Poisson coefficient is high. To understand this result, we perform three runs with increasing values of Poisson ratio (0.2, 0.3 and 0.4), while keeping all other parameters constant. The results show that when $\nu$ is increased the effective normal stress is increased. This compacts the soil and leads to the increase of the shear strength. Fig. 13 shows high variability of the outputs with respect to $\nu$, which confirms the results of the Sobol indices. Similar behavior can be observed in Fig. 13 for the marginal effect of $\varphi'$, indicating also that there is less risk of landslide when the friction angle is high. This is physically plausible because high values of $\varphi'$ correspond to high critical values of shear stress. $K_s(l)$ has also an increasing effect on $\overline{LFS}$ and decreasing effect on $A^{LFS}$. This indicates that there is less risk of landslide when the hydraulic conductivity of the lower layer of soil is high. This is also coherent with the physics, because high values of $K_s(l)$ lead to more infiltration to the lower layer of soil and less storage in the top layer. This reduces the additional stresses related to the weight of water. $\overline{LFS}$ (reps. $A^{LFS}$) is increasing (resp. decreasing) with $c'$. Thus the slope could be more stable when $c'$ is high. This is also fully coherent because when $c'$ is high the Mohr-Coulomb failure envelope is shifted upward.

### 4.6. Uncertainty quantification with PCE

The PCE surrogate model can be effectively used to quantify the uncertainties of the outputs (i.e., $\overline{LFS}$ and $A^{LFS}$) for a given uncertainty in the model inputs. Thus, we consider deterministic values of the significant parameter (i.e., $\nu, \varphi', K_s(l)$ and $c'$) as given in Table 4. We assume that these parameters are prone to 10 % uncertainty. The corresponding ranges of variability of the parameters are given in Table 4. The uncertainty of the model outputs is defined as the difference between the model outputs obtained with the deterministic parameters and the mean estimates of these outputs using stochastic parameters (Shahane et al., 2019). The uncertainty is calculated via two independent evaluations of the outputs. The first one is obtained using the deterministic values of the parameters, as given in Table 4. The second evaluation is obtained by considering 500 samples of the parameters over their ranges of variability. In order to reduce the CPU time, all the results are obtained using the PCE surrogate model. Advanced techniques can be found in Ji et al., (2019, 2020), Liao and Ji (2021) and Ji and Wang (2022). The results of the uncertainty quantification are given in Fig. 14. The figure shows that the resulting uncertainty on $\overline{LFS}$ and $A^{LFS}$ at three different time outputs. The uncertainty on $\overline{LFS}$ is quite small (about 0.2 %). This small value indicates that $\overline{LFS}$ cannot be used as metric for evaluating uncertainties in model predictions of soil stability. This can be confirmed by investigating the uncertainty on $A^{LFS}$, as in Fig. 14. The uncertainty on $A^{LFS}$ is about 4 %, for an uncertainty in the model inputs of 10 %.

Fig. 15 depicts the map of the uncertainty on LFS at t = 15 h. The highest uncertainty is about 5 %, which is coherent with the results of the uncertainty on $A^{LFS}$. Fig. 15 shows that the uncertainty on LFS is small in large space of the domain, except the zone where the failure could initiate. The large area of small uncertainties in Fig. 15 confirms the reason for the small uncertainty on $\overline{LFS}$ .

For more relevant analysis of the uncertainty on slope stability, we assume the landslide can occur when $A^{LFS}$ is greater than 10 % of the area of investigated zone. This approach could be relevant when the model is used for decision-making purposes. In our case, the area of investigated zone is about 113 $m^2$. Thus, the landslide is supposed to occur when $A^{LFS}$ is greater than 11.3. The deterministic simulation gives a value of $A^{LFS}$ of 14.9, indicating that the landslide will occur. Among the 500 stochastic simulations, 106 simulations provide inaccurate prediction, as they give value of $A^{LFS}$ less 11.3. This represents about 21 % of the total number of simulations. This result indicates that by selecting randomly the parameters over their range of variability, there is 21 % probability to obtain inaccurate prediction on the slope stability.

## 5. UA under more realistic conditions: wetting path of the retention curves and prior knowledge about soil type

The results of the previous section are based on a hypothetical benchmark that does not take into account various aspects related to RILS. However, it is known that the results of the UA depend on the variability of the uncertain parameters and the assumptions of the studied case. This section aims at performing the UA of RILS under more

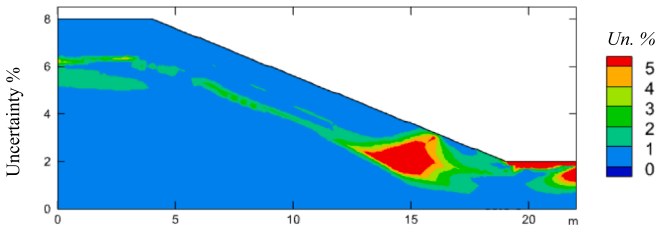


**Fig. 15.** Results of the uncertainty quantification analysis: Map of the uncertainty of LFS. The uncertainty is evaluated as the difference between the deterministic and stochastic values of LFS. The stochastic value is obtained as average of 500 stochastic simulations.

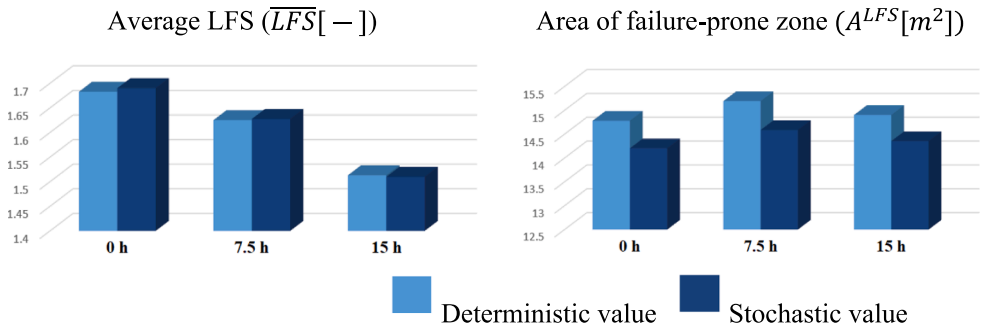


**Fig. 14.** Results of the uncertainty quantification analysis: difference between the deterministic and stochastic values of $\overline{LFS}$ and $A^{LFS}$ at t = 15 h. The stochastic values are obtained as the average value of 500 simulations performed with the PCEs surrogate model.

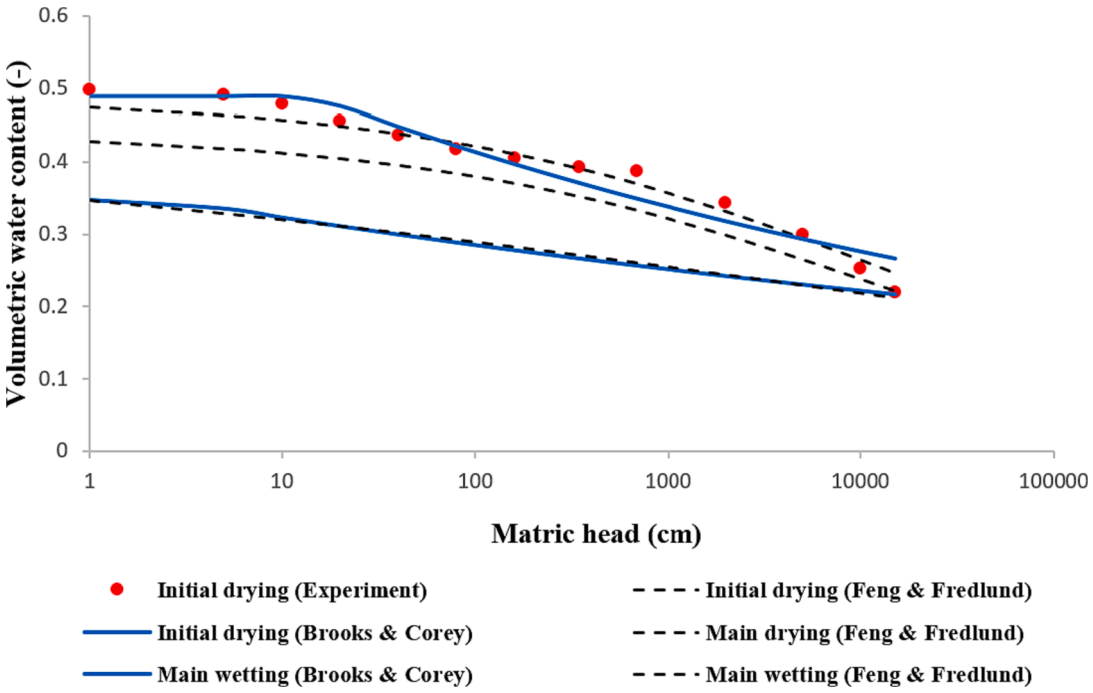


**Fig. 16.** Evaluation of the wetting path of the water content-pressure head retention curve.

**Table 5**
The ranges of variability of the wetting Brooks and Corey parameters obtained by deriving the wetting paths of the retention curves available in UNSODA data.

| Symbol | Units | High-level value | Low-level value |
|---|---|---|---|
| $\theta_s$ | – | 0.4 | 0.24 |
| $\theta_r$ | – | 0.09 | 0.01 |
| $K_S$ | cm/h | 5 | 1 |
| $\alpha_{BC}$ | 1/cm | 0.15 | 0.01 |
| $n_{BC}$ | – | 0.48 | 0.02 |
| $E$ | MPa | 40 | 8 |
| $\varphi'$ | ° | 30 | 24 |
| $c'$ | kPa | 6 | 3 |

realistic conditions. The following 3 aspects are considered in this section:

i. While in the hypothetical benchmark the drying path of the retention curves is used, it is known that the retention curves are hysteretic and the inclusion of the wetting branch of these curves can influence the results of the slope-stability analysis. Therefore, one of the objectives of this section is to perform the UA while considering the wetting path of the retention curves.
ii. The results of the hypothetical case are obtained under the assumption that all parameters are random without being known beforehand and the ranges of these parameters are determined by trial and error to ensure the significance of the model outputs. In this section, the aim is to perform the UA under for a specific soil type. In this case, more plausible ranges of parameters can be considered.
iii. The proposed strategy of UA is based on a 2-step technique. In the second step of this technique, the insignificant parameters are considered constant (i.e. the uncertainties of these parameters are neglected). This section is also concerned with investigating the validity of this approach. We therefore consider a new test case in which the geometry, boundary and initial conditions are the same as in the hypothetical benchmark (Fig. 2). However, in the new test case, the soil is assumed to consist of a single layer of sandy loam (i.e. a homogenous domain). This assumption makes it possible to reduce the number of parameters and investigate the validity of the proposed UA strategy, as will be explained later.

In order to obtain physical ranges for the uncertainties on the Brooks and Corey parameters, we use the data from UNSODA (UNsaturated SOil hydraulic DAtabase). UNSODA viewer is used for an easy access to the data (Seki et al., 2023). We use all the data for laboratory experiments under drying conditions available in UNSODA (98 sandy loam samples). The wetting branch of each sample is calculated as follows (Johari and Hooshmand Nejad, 2018):

- The data of the water retention curve is fitted with the Brooks and Corey model. This option is available in the UNSODA viewer using "SWRC Fit" (Seki et al., 2023). The fitted Brooks and Corey curve represents the initial drying curve.
- The initial drying curve is fitted with the Feng and Fredlund (1999) scaling model. The equations of this model are given in Appendix B. This allows for obtaining the curve-fitting parameters of the initial drying curve $(b_i, c_i and d_i)$.
- The main drying curve is then calculated by changing the parameter representing the saturated water content (see Appendix B).
- The wetting branch of the retention curve is then obtained by changing the parameters of the Feng and Fredlund (1999) model that governs the slope and the location of the curve using the distance and the slope ratio between the two boundary curves
- The main wetting curve is then fitted with the Brooks and Corey model to obtain the corresponding parameters.

This procedure is applied for all the samples of sandy loam available in UNSODA with full dataset (98 samples). A PYTHON code has been developed to obtain the wetting branches of these retention curves. This procedure allows for obtaining the wetting Brooks and Corey parameters for all the samples and thus the ranges of variability of these parameters. An example of the results is represented in Fig. 16. The obtained ranges of parameters are given in Table 5.

It is known that the Poisson's ratio has a smaller range of variation compared to the other mechanical parameters of the soil. For this reason, the Poisson's coefficient is assumed to be constant here ($\nu = 0.3$).

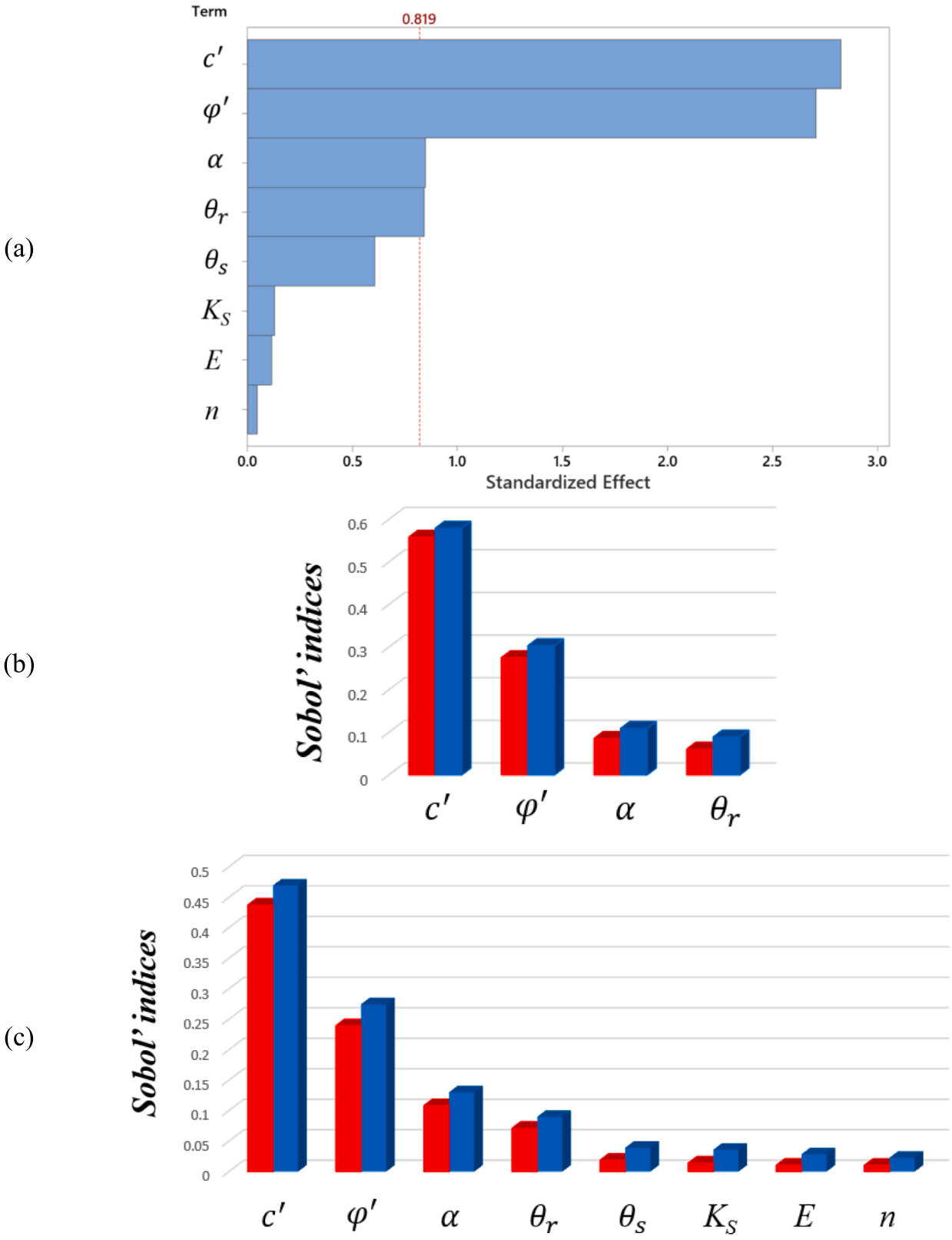


**Fig. 17.** (a) Pareto chart representing the standardized effects of parameters on the area of failure-prone zone ($A^{LFS}$), (b) First-order (red bars) and total (blue bars) Sobol indices indicating the sensitivity of $A^{LFS}$ to the most significant parameters ($c'$, $\varphi'$, $\alpha_{BC}$ and $\theta_r$). (c) First-order (red bars) and total (bleu bars) Sobol indices indicating the sensitivity of $A^{LFS}$ to all parameters based on GSA without the screening technique. All results correspond to the end of the rainfall event (i.e.. $t = 15h$).

The uncertainties related to other mechanical parameters (i.e. Young's modulus, cohesion coefficient and friction angle) are chosen to be physically plausible with the type of soil (i.e. sandy loam). The ranges of variability of these parameters are given in Table 5.It is assumed that the precipitation events are the same as in the first test case. The data required for the UA is generated using the COMSOL model with the same computational mesh as for the first test case. We first run the new simulations with a 2-step strategy of UA proposed in this work (screening technique and then GSA). 36 runs of the model are used for the screening technique and 200 runs for the GSA. The hypothetical test case shows that the area of the failure-prone zone is more relevant for UA than the average LFS. For the sake of brevity, we therefore limit the discussion here to $A^{LFS}$. The results of the screening technique are shown in Fig. 17a. The figure shows the statistically significant parameters that are above the significance threshold of 0.42, which corresponds to a standardized effect of more than 0.819. For the sake of brevity, the results are given at the end of the rainfall event, but the results are the same for all time steps. Fig. 17a shows that the most important parameters are $c'$, $\varphi'$, $\alpha_{BC}$ and $\theta_r$. We then perform a GSA by assuming these most important parameters as uncertain and other parameters as certain. For each certain parameter, the mean value of its variability range is used as a deterministic value. For the uncertain parameters, the same ranges of variability are used as for the screening technique. The accuracy of the PCE surrogate model is verified in the same way as in Fig. 8, but the results are not show for the sake of brevity. The results of the GSA are shown in Fig. 17b. This figure shows that even when the interactions between these parameters are taken into account, $c'$ is the most important parameter, followed by $\varphi'$ and $\alpha_{BC}$. Low sensitivity is observed for $\theta_r$. The results are coherent with the analytical expression of the factor of safety under infinite slope assumption given in Appendix A.

The results of this test case are different from the previous one. It is clear that in this test case with sandy loam soil, the slop stability is more sensitive to the mechanical parameters than hydraulic parameters. When uncertainty on the Poisson's ratio is neglected, the most sensitive mechanical parameters are the cohesion soil shear resistance ($c'$ and $\varphi'$). Regarding the hydraulic parameters, the slop stability appears to be sensitive as it is observed in the first test case. This makes sense, because the domain is homogenous and imposed flux is imposed at the top surface of the soil, thus the water content distribution is not sensitive to the hydraulic conductivity.

The results of the GSA are obtained while neglecting the uncertainties on the insignificant parameters ($\theta_s$, $K_S$, $n_{BC}$ and $E$). In order to verify this assumption, we perform a GSA while considering all parameters as random. We should mention that in this case, where the number of uncertain parameters is high, GSA requires a large number of simulations to create an accurate surrogate model with the polynomial chaos expansion (PCE). For this reason we have considered a homogenous domain that makes it possible to reduce the number of uncertain parameters to 8 instead of 14 in the case of a heterogeneous domain. With 8 uncertain parameters, an accurate surrogate model is obtained with 600 runs of the forward model. The results of the GSA performed with 8 uncertain parameters are given in Fig. 17c.

This Figure confirms the results obtained with the the 2-step technique. The most important parameters are $c'$, $\varphi'$, $\alpha_{BC}$ and $\theta_r$. So the main conclusion is that the results do not change even if we consider all parameters as random, because these parameters are insignificant, as the screening technique shows. We should mention that the CPU time for 600 runs is about 10 days, while it is about 3 days for the 236 runs required with the 2-step method proposed in this paper.

## 6. Conclusion

A new integrated framework was proposed for uncertainty analysis of rainfall-induced landslides on slopes, which is a challenging issue due to high dimensionality, model nonlinearity, and high computational overheads of forward simulations. Appropriate techniques were implemented and coupled together in a sequential way to allow for addressing challenges and performing accurate and efficient uncertainty analysis. Thus, as a first step a finite element model was developed with COMSOL®, where appropriate space discretization and time integration techniques were used to optimize the computational costs of the forward simulations. The concept of local factor of safety (LFS) was used for the assessment of landslide susceptibility, due to its flexibility, reliability and simplicity. Global metrics were used for performing the analysis. Thus, average LFS and area of the zone where LFS is less than one were defined as main outputs. A screening technique was applied to identify the most significant parameters, while neglecting interactions between parameters. A Plackett Burman design was used to perform the screening technique. A global sensitivity analysis with the variance-based technique was performed to rank the remaining significant parameters by order of importance. Sobol indices are used as sensitivity indicators because they allows for considering interactions between parameters. A surrogate model is used to render the sensitivity analysis practical. PCEs were used for building the surrogate model due to their accuracy and because they allow for forward evaluation of the Sobol indices without any further treatments. Both total and first-order Sobol indices were investigated in order to evaluate the interactions between parameters. An uncertainty quantification analysis, based on stochastic simulations, was then performed with the PCEs surrogate model. It aims at quantifying the uncertainties of outputs for prescribed uncertainties in inputs.

A hypothetical benchmark at 100 m scale is considered. The soil is assumed to be heterogeneous with two different layers. Preliminary analysis showed that local LFS cannot be used as metrics for the sensitivity analysis, as they can be sensitive to the computational mesh and numerical parameters. Reliable results were obtained with global metrics as the overall average of LFS and the area of the failure-prone zone.

The soil properties, with a total number of 14 parameters, were considered as uncertain parameters. The ranges of variability of these parameters are defined by a trial and error procedure in order to ensure the significance of the model outputs. The screening technique allowed for eliminating 10 insignificant parameters out of these. For this benchmark and the ranges of parameters under investigation, the most significant parameters identified were the Poisson ratio, the hydraulic conductivity of the lower layer of soil, the friction angle and the effective cohesion coefficient.

A global sensitivity analysis was then performed on the 4 remaining significant parameters. The results of the Sobol indices indicated that the variability of the model outputs is first related to the Poisson coefficient, then to the friction angle and hydraulic conductivity of the soil, and finally to the effective cohesion coefficient. The results of the suggested analysis are coherent with the concept of global factor of safety based either on the infinite slope or infinite depth assumptions. Spatial variability of uncertainties is investigated using the spatial maps of the Sobol indices. The marginal effects of the parameters on the model outputs are investigated. The results show that the risk of landslide increases when the values of these parameters decrease. Finally, the PCE is used for performing stochastic simulations for uncertainty quantification. The results show that, if the parameters are randomly with 10 % uncertainty selected over their range of variability, the probability of inaccurate prediction on landslide occurrence is about 21 %.

It is relevant nothing that the results of the uncertainty propagation analysis are not generic because they depend both on the variability of the uncertain parameters and on the investigated case. Thus, while apply the proposed strategy of uncertainty analysis to more realistic configuration when the wetting branch of the retention curves are considered and when the type of the soil is well defined (sandy loam). The ranges of variability of the parameters are chosen to correspond to sandy loam. Under these more realistic conditions, the results are different from those obtained with the hypothetical benchmark. The

most important parameters become the cohesion coefficient, friction angle and air entry pressure head, respectively.

The uncertainty analysis framework suggested in this work is applied for cases where the soil parameters are uncertain, but the approach is generic and can be applied to other kinds of uncertainties such as the rainfall intensity, the slope angle, and soil heterogeneity. A hypothetical benchmark is investigated, but the approach can be used for real-field studies. Specific attention should be given to the computational costs for data generation. The mechanical model is relatively simple, but the analysis can be extended to a fully coupled poroelastic model with elasto-plastic deformation. However, again an efficient forward model should be used to deal with the computational overheads for data generation.

## CRediT authorship contribution statement

**Rashad Abbasov:** . **Marwan Fahs:** . **Anis Younes:** . **Hossein Nowamooz:** Methodology. **Knut Jørgen Måløy:** . **Renaud Toussaint:** Writing – review & editing, Supervision, Methodology, Funding acquisition, Conceptualization.

## Declaration of competing interest

The authors declare that they have no known competing financial interests or personal relationships that could have appeared to influence the work reported in this paper.

## Data availability

No data was used for the research described in the article.

## Acknowledgments

Authors would like to acknowldge the suport of the state program on increasing the international competitiveness of the higher education system in the Republic of Azerbaijan for 2019-2023. The authors would also like to thank Professor François Lehmann from the university of Strasbourg for his help during the revision process. We also acknowledge and are grateful for the support of the IRP France-Norway D-FFRACT, of CNRS, Universities of Strasbourg, Oslo and the CNRS MITI program. We thank the Research Council of Norway through its Centres of Excellence funding scheme, project number 262644.

## Appendix A:. Evaluation of the local factor of safety

*LFS* is defined as the ratio of resisting shear strength ($\tau^*$) to gravitationally driven shear stress ($\tau$) in the failure direction. Based on the Mohr-Coulomb criterion, the resisting shear strength is given by:

$$\tau^* = cos^2(\varphi^{'})\cdot\left(c^{'} + {\sigma_{eff}}^{I}\cdot tan(\varphi^{'})\right) \tag{A1}$$

where $c^{'}$ parameter represents the effective soil cohesion and $\varphi^{'}[-]$ is the effective friction angle. The effective stress ${\sigma_{eff}}^{I}$ is the centre of the Mohr circles.

The shear stress ($\tau$) can be expressed in terms of the eigenvalues of the stress tensor as follows:

$$\tau = cos(\varphi^{'}).{\sigma_{eff}}^{II} \tag{A2}$$

Thus, the general form of the LFS is given by:

$$LFS = \frac{cos(\varphi^{'})\cdot\left(c^{'} + {\sigma_{eff}}^{I}\cdot tan(\varphi^{'})\right)}{{\sigma_{eff}}^{II}} \tag{A3}$$

The factor of safety under infinite slope assumption is given by (Baum et al., 2010):

$$FS(Z,t) = \frac{tan(\varphi^{'})}{tan(\delta)} + \frac{c^{'} - \gamma_w.h\cdot tan(\varphi^{'})}{\gamma_s.Z.sin(\delta).\cos(\delta)} \tag{A4}$$

Where, *FS* is the factor of safety, $Z$ is the depth of soil, $t$ is the time, $\delta$ is the slope's inclination angle, $\gamma_w$ is the unit weight of water, $\gamma_s$ is the unit weight of soil and $h$ is the water pressure head.

Under infinite depth assumption, the minimum global factor of safely is given by:

$$LFS_{min} = \frac{1+\nu}{1-\nu} sin(\varphi^{'}) \tag{A5}$$

## Appendix B:. Evaluation of wetting branch of the retention curve

The Brooks and Corey initial drying curve is first fitted with the following model:

$$\theta_i(h) = \frac{\theta_s b_i + c_i h^{d_i}}{b_i + h^{d_i}} \tag{B1}$$

This allows for obtaining the fitting parameters $b_i$, $c_i$ and $d_i$.

The water content at the main drying curve can be calculated by changing the parameter representing the water content at saturation ($\theta_u = 0.9\theta_s$). This leads to the following equation

$$\theta_d(h) = \frac{\theta_u b_i + c_i h^{d_i}}{b_i + h^{d_i}} \tag{B2}$$

The wetting branch of the retention curve is obtained by using fitting parameters $b_w$, $c_w$ and $d_w$ that are calculated from initial dry fitting parameters as follows:

$$c_w = c_i \tag{B3}$$

$$b_w = \left[\frac{b_i}{\left(10^{D_{SL}}\right)^{d_i}}\right]^{\frac{1}{R_{SL}}} \tag{B4}$$

$$d_w = \frac{d_i}{R_{SL}} \tag{B5}$$

where $D_{SL}$ is the distance between the main dry and main wet curves and $R_{SL}$ is the slope ration between these curves. For sandy loam we assume $D_{SL} = 0.25$ and $R_{SL} = 2.5$ as suggested in Johari and Hooshmand Nejad (2018).

The wetting branch of the retention curve is given by:

$$\theta_w(h) = \frac{\theta_u b_w + c_w h^{d_w}}{b_w + h^{d_w}} \tag{B6}$$

## References


Almeida, S., Holcombe, E.A., Pianosi, F., Wagener, T., 2017. Dealing with deep uncertainties in landslide modelling for disaster risk reduction under climate change. Nat Hazards Earth Syst Sci 17, 225–241. https://doi.org/10.5194/nhess-17-225-2017.

Asher, M.J., Croke, B.F.W., Jakeman, A.J., Peeters, L.J.M., 2015. A review of surrogate models and their application to groundwater modeling: Surrogates of groundwater models. Water Resour Res 51, 5957–5973. https://doi.org/10.1002/2015WR016967.

Ayaz M, Toussaint R, Schäfer G, Måløy KJ. Gravitational and Finite-Size Effects On Pressure Saturation Curves During Drainage. Water Resour Res 2020;56. 10.1029/2019WR026279.

Baum, R.L., Godt, J.W., Savage, W.Z., 2010. Estimating the timing and location of shallow rainfall-induced landslides using a model for transient, unsaturated infiltration. J Geophys Res 115, F03013. https://doi.org/10.1029/2009JF001321.

Ben-Zeev, S., Goren, L., Parez, S., Toussaint, R., Clément, C., Aharonov, E., 2017. The combined effect of buoyancy and excess pore pressure in facilitating soil liquefaction. poromechanics VI. American Society of Civil Engineers, Paris, France, pp. 107–116.

Ben-Zeev, S., Aharonov, E., Toussaint, R., Parez, S., Goren, L., 2020. Compaction front and pore fluid pressurization in horizontally shaken drained granular layers. Phys Rev Fluids 5, 054301. https://doi.org/10.1103/PhysRevFluids.5.054301.

Bishop, A.W., 1959. The principle of effective stress. Tek Ukebl 106, 859–863.

Cai, J.-S., Yeh, T.-C.-J., Yan, E.-C., Hao, Y.-H., Huang, S.-Y., Wen, J.-C., 2017. Uncertainty of rainfall-induced landslides considering spatial variability of parameters. Comput. Geotech. 87, 149–162. https://doi.org/10.1016/j.compgeo.2017.02.009.

Chiu, Y.-Y., Chen, H.-E., Yeh, K.-C., 2019. Investigation of the influence of rainfall runoff on shallow landslides in unsaturated soil using a mathematical model. Water 11, 1178. https://doi.org/10.3390/w11061178.

Clément, C., Toussaint, R., Stojanova, M., Aharonov, E., 2018. Sinking during earthquakes: Critical acceleration criteria control drained soil liquefaction. Phys Rev E 97, 022905. https://doi.org/10.1103/PhysRevE.97.022905.

Fajraoui, N., Fahs, M., Younes, A., Sudret, B., 2017. Analyzing natural convection in porous enclosure with polynomial chaos expansions: Effect of thermal dispersion, anisotropic permeability and heterogeneity. Int. J. Heat Mass Transf. 115, 205–224. https://doi.org/10.1016/j.ijheatmasstransfer.2017.07.003.

Fang, Y., Su, Y., 2020. On the use of the global sensitivity analysis in the reliability-based design: Insights from a tunnel support case. Comput. Geotech. 117, 103280 https://doi.org/10.1016/j.compgeo.2019.103280.

Feng, M., Fredlund, D.G., 1999. Hysteretic influence associated with thermal conductivity sensor measurements. In: Proceedings of the 52nd Canadian geotechnical conference, Regina, Sask.

Glen, G., Isaacs, K., 2012. Estimating Sobol sensitivity indices using correlations. Environ. Model. Softw. 37, 157–166. https://doi.org/10.1016/j.envsoft.2012.03.014.

Goren, L., Toussaint, R., Aharonov, E., Sparks, D.W., Flekkøy, E., 2013. A General Criterion for Liquefaction in Granular Layers with Heterogeneous Pore Pressure. Poromechanics V. American Society of Civil Engineers, Vienna, Austria, pp. 415–424.

Greco, R., Pagano, L., 2017. Basic features of the predictive tools of early warning systems for water-related natural hazards: examples for shallow landslides. Nat Hazards Earth Syst Sci 17, 2213–2227. https://doi.org/10.5194/nhess-17-2213-2017.

Guo, L., Fahs, M., Hoteit, H., Gao, R., Shao, Q., 2021. Uncertainty analysis of seepage-induced consolidation in a fractured porous medium. Comput. Model. Eng. Sci. 129 (279–97) https://doi.org/10.32604/cmes.2021.016619.

Haque, U., Blum, P., da Silva, P.F., Andersen, P., Pilz, J., Chalov, S.R., et al., 2016. Fatal landslides in Europe. Landslides 13, 1545–1554. https://doi.org/10.1007/s10346-016-0689-3.

Highland, L., Bobrowsky, P.T., 2008. The landslide handbook: a guide to understanding landslides. U.S. Geological Survey, Reston, Va.

Homma, T., Saltelli, A., 1996. Importance measures in global sensitivity analysis of nonlinear models. Reliab. Eng. Syst. Saf. 52, 1–17. https://doi.org/10.1016/0951-8320(96)00002-6.

Hungr, O., Leroueil, S., Picarelli, L., 2014. The Varnes classification of landslide types, an update. Landslides 11, 167–194. https://doi.org/10.1007/s10346-013-0436-y.

Iverson, R.M., Reid, M.E., 1992. Gravity-driven groundwater flow and slope failure potential: 1. Elastic Effective-Stress Model. Water Resour Res 28, 925–938. https://doi.org/10.1029/91WR02694.

Ji, J., Zhang, C., Gao, Y., Kodikara, J., 2019. Reliability-based design for geotechnical engineering: An inverse FORM approach for practice. Comput. Geotech. 111, 22–29. https://doi.org/10.1016/j.compgeo.2019.02.027.

Ji, J., Wang, C.-W., Gao, Y., Zhang, L., 2021. Probabilistic investigation of the seismic displacement of earth slopes under stochastic ground motion: a rotational sliding block analysis. Can Geotech J 58, 952–968. https://doi.org/10.1139/cgj-2020-0252.

Ji, J., Wang, L.-P., 2022. Efficient geotechnical reliability analysis using weighted uniform simulation method involving correlated nonnormal random variables. J Eng Mech 148, 06022001. https://doi.org/10.1061/(ASCE)EM.1943-7889.0002101.

Johari, A., Hooshmand, N.A., 2018. An Approach to estimate wetting path of soil-water retention curve from drying path. Iran J Sci Technol Trans Civ Eng 42, 85–89. https://doi.org/10.1007/s40996-017-0074-z.

Johari, A., Talebi, A., 2019. Stochastic analysis of rainfall-induced slope instability and steady-state seepage flow using random finite-element method. Int J Geomech 19, 04019085. https://doi.org/10.1061/(ASCE)GM.1943-5622.0001455.

Jouniaux, L., Allègre, V., Toussaint, R., Zyserman, F., 2020. Saturation dependence of the streaming potential coefficient. In: Grobbe, N., Revil, A., Zhu, Z., Slob, E. (Eds.), Geophysical Monograph Series, 1st ed.,. Wiley, pp. 73–100. https://doi.org/10.1002/9781119127383.ch5.

Kasama, K., Furukawa, Z., Hu, L., 2021. Practical reliability analysis for earthquake-induced 3D landslide using stochastic response surface method. Comput. Geotech. 137, 104303 https://doi.org/10.1016/j.compgeo.2021.104303.

Khalaj, S., BahooToroody, F., Mahdi Abaei, M., BahooToroody, A., De Carlo, F., Abbassi, R., 2020. A methodology for uncertainty analysis of landslides triggered by an earthquake. Comput. Geotech. 117, 103262 https://doi.org/10.1016/j.compgeo.2019.103262.

Koohbor, B., Fahs, M., Ataie-Ashtiani, B., Belfort, B., Simmons, C.T., Younes, A., 2019. Uncertainty analysis for seawater intrusion in fractured coastal aquifers: Effects of fracture location, aperture, density and hydrodynamic parameters. J. Hydrol. 571, 159–177. https://doi.org/10.1016/j.jhydrol.2019.01.052.

Lanni, C., McDonnell, J., Hopp, L., Rigon, R., 2013. Simulated effect of soil depth and bedrock topography on near-surface hydrologic response and slope stability: The role of bedrock topography on slope stability. Earth Surf Process Landforms 38, 146–159. https://doi.org/10.1002/esp.3267.

Liao, W., Ji, J., 2021. Time-dependent reliability analysis of rainfall-induced shallow landslides considering spatial variability of soil permeability. Comput. Geotech. 129, 103903 https://doi.org/10.1016/j.compgeo.2020.103903.

Lu, N., Likos, W.J., 2006. Suction stress characteristic curve for unsaturated soil. J Geotech Geoenviron Eng 132, 131–142. https://doi.org/10.1061/(ASCE)1090-0241(2006)132:2(131).

Lu, N., Godt, J.W., Wu, D.T., 2010. A closed-form equation for effective stress in unsaturated soil: Effective Stress in Unsaturated Soil. Water Resour Res. 46. https://doi.org/10.1029/2009WR008646.
Lu, N., Griffiths, D.V., 2004. Profiles of steady-state suction stress in unsaturated soils. J Geotech Geoenviron Eng 130, 1063–1076. https://doi.org/10.1061/(ASCE)1090-0241(2004)130:10(1063).
Lu, N., Likos, W.J., 2004. Unsaturated soil mechanics. J. Wiley, Hoboken, N.J.
Lu, N., Şener-Kaya, B., Wayllace, A., Godt, J.W., 2012. Analysis of rainfall-induced slope instability using a field of local factor of safety. Water Resour Res. 48 https://doi.org/10.1029/2012WR011830.
Mandal, P., Sarkar, S., 2021. Estimation of rainfall threshold for the early warning of shallow landslides along National Highway-10 in Darjeeling Himalayas. Nat Hazards 105, 2455–2480. https://doi.org/10.1007/s11069-020-04407-9.
Menon, V., Kolathayar, S., 2022. Review on landslide early warning system: A brief history, evolution, and controlling parameters. In: Kolathayar, S., Pal, I., Chian, S.C., Mondal, A. (Eds.), Civil Engineering for Disaster Risk Reduction. Springer Singapore, Singapore, pp. 129–145. https://doi.org/10.1007/978-981-16-5312-4_10.
Mitarai, N., Nori, F., 2006. Wet granular materials. Adv. Phys. 55, 1–45. https://doi.org/10.1080/00018730600626065.
Moradi, S., Huisman, J., Class, H., Vereecken, H., 2018. The effect of bedrock topography on timing and location of landslide initiation using the local factor of safety concept. Water 10, 1290. https://doi.org/10.3390/w10101290.
Moura, M., Fiorentino, E.-A., Måløy, K.J., Schäfer, G., Toussaint, R., 2015. Impact of sample geometry on the measurement of pressure-saturation curves: Experiments and simulations. Water Resour Res 51, 8900–8926. https://doi.org/10.1002/2015WR017196.
Niebling, M.J., Flekkøy, E.G., Måløy, K.J., Toussaint, R., 2010. Mixing of a granular layer falling through a fluid. Phys Rev E 82, 011301. https://doi.org/10.1103/PhysRevE.82.011301.
Niebling, M.J., Toussaint, R., Flekkøy, E.G., Måløy, K.J., 2012. Dynamic aerofracture of dense granular packings. Phys Rev E 86, 061315. https://doi.org/10.1103/PhysRevE.86.061315.
Pan, Q.-J., Leung, Y.-F., Hsu, S.-C., 2021. Stochastic seismic slope stability assessment using polynomial chaos expansions combined with relevance vector machine. Geosci. Front. 12, 405–414. https://doi.org/10.1016/j.gsf.2020.03.016.
Rajabi, M.M., Fahs, M., Panjehfouladgaran, A., Ataie-Ashtiani, B., Simmons, C.T., Belfort, B., 2020. Uncertainty quantification and global sensitivity analysis of double-diffusive natural convection in a porous enclosure. Int. J. Heat Mass Transf. 162, 120291 https://doi.org/10.1016/j.ijheatmasstransfer.2020.120291.
Razavi, S., Gupta, H.V., 2016. A new framework for comprehensive, robust, and efficient global sensitivity analysis: 1. Theory. Water Resour Res 52, 423–439. https://doi.org/10.1002/2015WR017558.
Sahu, Q., Fahs, M., Hoteit, H., 2023. Optimization and uncertainty quantification method for reservoir stimulation through carbonate acidizing. ACS Omega 8, 539–554. https://doi.org/10.1021/acsomega.2c05564.
Saltelli, A., 2008. editor. Global sensitivity analysis: the primer. John Wiley, Chichester, England; Hoboken, NJ.
Sandoval, L., Riva, M., Colombo, I., Guadagnini, A., 2022. Sensitivity analysis and quantification of the role of governing transport mechanisms and parameters in a gas flow model for low-permeability porous media. Transp Porous Med 142, 509–530. https://doi.org/10.1007/s11242-022-01755-x.
Schilirò, L., Esposito, C., Scarascia, M.G., 2015. Evaluation of shallow landslide-triggering scenarios through a physically based approach: an example of application in the southern Messina area (northeastern Sicily, Italy). Nat Hazards Earth Syst Sci 15, 2091–2109. https://doi.org/10.5194/nhess-15-2091-2015.
Seki, K., Toride, N., Van Genuchten, M.T., 2023. Evaluation of a general model for multimodal unsaturated soil hydraulic properties. Journal of Hydrology and Hydromechanics 71, 22–34. https://doi.org/10.2478/johh-2022-0039.
Shahane, S., Aluru, N.R., Vanka, S.P., 2019. Uncertainty quantification in three dimensional natural convection using polynomial chaos expansion and deep neural networks. Int. J. Heat Mass Transf. 139, 613–631. https://doi.org/10.1016/j.ijheatmasstransfer.2019.05.014.
Shao, W., Bogaard, T., Bakker, M., 2014. How to use COMSOL multiphysics for coupled dual-permeability hydrological and slope stability modeling. Procedia Earth Planet. Sci. 9, 83–90. https://doi.org/10.1016/j.proeps.2014.06.018.
Shao, W., Bogaard, T.A., Bakker, M., Greco, R., 2015. Quantification of the influence of preferential flow on slope stability using a numerical modelling approach. Hydrol Earth Syst Sci 19, 2197–2212. https://doi.org/10.5194/hess-19-2197-2015.
Shao, Q., Younes, A., Fahs, M., Mara, T.A., 2017. Bayesian sparse polynomial chaos expansion for global sensitivity analysis. Comput. Methods Appl. Mech. Eng. 318, 474–496. https://doi.org/10.1016/j.cma.2017.01.033.
Sobol, I.M., 1993. Sensitivity estimates for nonlinear mathematical models. Model Comput Exp 2, 407–414.
Sudret, B., 2008. Global sensitivity analysis using polynomial chaos expansions. Reliab. Eng. Syst. Saf. 93, 964–979. https://doi.org/10.1016/j.ress.2007.04.002.
Toussaint, R., Måløy, K.J., Méheust, Y., Løvoll, G., Jankov, M., Schäfer, G., et al., 2012. Two-phase flow: Structure, upscaling, and consequences for macroscopic transport properties. Vadose Zone J. 11 https://doi.org/10.2136/vzj2011.0123.
Travelletti, J., Malet, J.-P., Delacourt, C., Allemand, P., Schmittbuhl, J., Toussaint, R., 2011. Performance of image correlation techniques for landslide displacement monitoring. landslide science and practice: Early warning. Instrumentation and Monitoring. 2 https://doi.org/10.1007/978-3-642-31445-2-28.
Travelletti, J., Delacourt, C., Allemand, P., Malet, J.-P., Schmittbuhl, J., Toussaint, R., et al., 2012. Correlation of multi-temporal ground-based optical images for landslide monitoring: Application, potential and limitations. ISPRS J. Photogramm. Remote Sens. 70, 39–55. https://doi.org/10.1016/j.isprsjprs.2012.03.007.
Tsai, T.-L., 2008. The influence of rainstorm pattern on shallow landslide. Environ Geol 53, 1563–1569. https://doi.org/10.1007/s00254-007-0767-x.
Tsai, T.-L., Wang, J.-K., 2011. Examination of influences of rainfall patterns on shallow landslides due to dissipation of matric suction. Environ Earth Sci 63, 65–75. https://doi.org/10.1007/s12665-010-0669-1.
Vanaja, K., Shobha Rani, R.H., 2007. Design of experiments: Concept and applications of plackett burman design. Clin. Res. Regul. Aff. 24, 1–23. https://doi.org/10.1080/10601330701220520.
Wang, J., Chi, S., Shao, X., Zhou, X., 2021. Determination of the mechanical parameters of the microstructure of rockfill materials in triaxial compression DEM simulation. Comput. Geotech. 137, 104265 https://doi.org/10.1016/j.compgeo.2021.104265.
Wirth, S.B., Glur, L., Gilli, A., Anselmetti, F.S., 2013. Holocene flood frequency across the Central Alps – solar forcing and evidence for variations in North Atlantic atmospheric circulation. Quat. Sci. Rev. 80, 112–128. https://doi.org/10.1016/j.quascirev.2013.09.002.
Yang, Z., Liu, C., Nie, R., Zhang, W., Zhang, L., Zhang, Z., et al., 2022b. Research on uncertainty of landslide susceptibility prediction—bibliometrics and knowledge graph analysis. Remote Sens. (Basel) 14, 3879. https://doi.org/10.3390/rs14163879.
Yang, Y.-S., Yeh, H.-F., Ke, C.-C., Chen, N.-C., Chang, K.-C., 2022a. Assessment of probability of failure on rainfall-induced shallow landslides at slope scale using a physical-based model and fuzzy point estimate method. Front Earth Sci 10, 957506. https://doi.org/10.3389/feart.2022.957506.
Yang, H.-Q., Zhang, L., Li, D.-Q., 2018. Efficient method for probabilistic estimation of spatially varied hydraulic properties in a soil slope based on field responses: A Bayesian approach. Comput. Geotech. 102, 262–272. https://doi.org/10.1016/j.compgeo.2017.11.012.
Zhang, L., Wu, F., Wei, X., Yang, H.-Q., Fu, S., Huang, J., et al., 2023. Polynomial chaos surrogate and bayesian learning for coupled hydro-mechanical behavior of soil slope. Rock Mechanics Bulletin 2, 100023. https://doi.org/10.1016/j.rockmb.2022.100023.
Zheng, H., Mooney, M., Gutierrez, M., 2023. Surrogate model for 3D ground and structural deformations in tunneling by the sequential excavation method. Comput. Geotech. 154, 105142 https://doi.org/10.1016/j.compgeo.2022.105142.